RESEARCH ARTICLE

WILEY

Development and validation of a lifting-line code associated with the vortex particle method software Dorothy

M.-A. Dufour[1,4] | G. Pinon[1] | E. Rivoalen[1,2] | F. Blondel[3] | G. Germain[4]

[1]Laboratoire Ondes et Milieux Complexes (LOMC) - Normandie Univ, UNIHAVRE, CNRS, Le Havre, France

[2]Laboratoire de Mécanique de Normandie (LMN) - Normandie Univ, INSA ROUEN, LMN, Rouen, France

[3]IFP Energies Nouvelles, Rueil-Malmaison, France

[4]Laboratoire d'Hydrodynamique Marine (LHyMar), IFREMER, Centre Manche Mer du Nord, Boulogne-sur-Mer, France

Correspondence
G. Pinon, Laboratoire Ondes et Milieux Complexes (LOMC) - Normandie Univ, UNIHAVRE, CNRS, 76600 Le Havre.
Email: gregory.pinon@univ-lehavre.fr

Funding information
Institut Français de Recherche pour l'Exploitation de la Mer; Région Normandie; Labex EMC3, Grant/Award Number: 10-LABX-0009; European Regional Development Fund

Abstract

This paper presents a lifting-line implementation in the framework of a Lagrangian vortex particle method (LL-VP). The novelty of the present implementation lies in the fluid particles properties definition and in the particles shedding process. In spite of mimicking a panel method, the LL-VP needs some peculiar treatments described in the paper. The present implementation converges rapidly and efficiently during the shedding sub-iteration process. This LL-VP method shows good accuracy, even with moderate numbers of sections. Compared to its panel or vortex filaments counterparts, more frequently encountered in the literature, the present implementation inherently accounts for the diffusion term of the Navier-Stokes equations, possibly with a turbulent viscosity model. Additionally, the present implementation can also account for more complex onset flows: upstream ambient turbulence and upstream turbine wakes. After validation on an analytical elliptic wing configuration, the model is tested on the Mexnext-III wind turbine application, for three reduced velocities. Accurate results are obtained both on the analytical elliptic wing and on the New MEXICO rotor cases in comparison with other similar numerical models. A focus is made on the Mexnext-III wake analysis. The numerical wake obtained with the present LL-VP is close to other numerical and experimental results. Finally, a last configuration with three tidal turbines in interaction is considered based on an experimental campaign carried out at the IFREMER wave and current flume tank. Enhanced turbine-wake interactions are highlighted, with favourable comparisons with the experiment. Hence, such turbine interactions in a farm are accessible with this LL-VP implementation, be it wind or tidal energy field.

KEYWORDS
CFD, lifting-line, vortex particle method, wake interaction, wind turbine

1 | INTRODUCTION

Decreasing the share of carbon-emitting energy sources in the energy mix is a top priority for mankind to mitigate climate change. Among the various low-carbon energy sources, both tidal and wind energy will play a significant role worldwide to achieve this objective. The basic principle of those technologies is extracting kinetic energy from a moving fluid, be it water or air. Both domains bring along questions and uncertainties that

need to be addressed. On the one hand, the development of floating offshore wind turbines raises questions about rotor unsteady loadings induced by the floating platform motions.[1] This is the reason why some filamentary and panel free vortex wake (FVW) codes have been re-developed for turbine modelling[2] and used since a couple of years.[1,3–6] Those FVW codes rely on the lifting-line (LL) theory for blades representation. This theory was first introduced by Prandtl in the early 20th century,[7] and it underwent modern developments for panel or filamentary FVW codes.[8,9] It remains relevant up to these days as giving accurate results together with a limited computational cost. On the other hand, tidal and wind farms deployment introduces new uncertainties due to turbine wake interactions. The extent to which upstream turbine wakes in an highly turbulent environment affect unsteady blade loads of the downstream turbines is still unclear. As this matter cannot be tackled by FVW codes, turbine arrays have mainly been studied through Eulerian computational fluid dynamics (CFD).[10–12] This is the reason why, to the authors viewpoint, a Navier-Stokes (NS) equations solver based on the Lagrangian vortex particle (VP) method can play an important role in tackling this issue. In the Eulerian fluid description, the position is fixed. Thus, a mesh representing the complete fluid domain is required. This results sometimes in costly computations. However, in the Lagrangian VP framework, only specific fluid particles carrying vorticity are tracked with their position being a function of time. Lagrangian VP then offers the possibility to solve NS equations with a limited computational cost. Furthermore, contrary to FVW approach, Lagrangian VP inherently accounts for the diffusion term in the NS equations and allows for turbine wake interactions. The vortex method dates back to 1931 with Rosenhead's[13] pioneering idea to transform a surface of discontinuity, which is a vortex line, into discretized vortices of appropriate vorticity, like in the Kelvin-Helmholtz or shear-layer instability. A renewed interest in the method occurred in the 1970s because of progresses in computational resources. At this time, the VP method was generalized for 3D problems and enhanced till reaching mature development stage.[14–18] Since then, several authors used the VP method for wind and tidal turbine modelling, citing a couple of studies as a matter of examples.[19–26] The present VP solver Dorothy, developed jointly by IFREMER and LOMC,[23,26–29] is part of this movement in turbine modelling. The need for a lean blade representation inside this VP solver was rapidly felt as critical, together with the need of accurate loads evaluation. As a consequence, an LL blade representation is developed and presented in this work. This approach follows recent studies using an LL adapted in Lagrangian VP solver[24,30,31] or hybrid FVW-VP method.[32] The present paper aims at contributing to these developments by offering new vortex particles definition and a new shedding process to smoothly adapt the lifting-line methodology in the VP framework.

In this paper, after the introductory section, the VP method background and core equations are first explained in Section 2. Some mathematical arguments are briefly reminded in Appendix A because they are key to understand the underlying principles of the VP method. The interested reader is invited to refer to the literature[15,17,18,33] where those aspects have been thoroughly studied. Second, the lifting-line implementation within Dorothy VP solver is presented in Section 3. This method is called here LL-VP. The important features are highlighted so that the reader can identify the difficulties, especially dedicated for coders willing to reuse the presented formulation. In Section 4, the present approach is validated against test cases of increasing complexity. As a starting point, an elliptic wing is studied in order to validate the developments. Then, wind turbine radial loads and near wake velocity profiles are evaluated on the Mexnext-III cases. Eventually, wake interactions for three tidal turbine models are computed and compared to experimental results. The concluding section highlights Dorothy LL-VP capability to simulate both wind and tidal turbines behaviours.

2 | LAGRANGIAN VORTEX PARTICLE METHOD IN THE DOROTHY SOLVER

Section 2.1 focuses first on presenting the basis of vortex method with regularized kernels. The transcription of the vortex method background into a particles framework is studied in Section 2.2. Eventually the Lagrangian vortex particle method set of equations, used in the Dorothy solver, is presented in Section 2.3. Some core challenges of the VP method that have been developed and thoroughly studied in the literature[15,17,18,33] are reminded in Appendix A.

2.1 | The vortex method

To start with, the fluid is assumed to be incompressible, which implies that the fluid density (ρ) is constant. The kinematic viscosity of the fluid (ν) is assumed to be constant. But some peculiar aspects dedicated to large eddy simulation (LES) modelling with a turbulent viscosity are added in Section 2.3. The fluid is not subjected to any outside force. The velocity vector and pressure scalar fields are respectively defined as $\vec{u} = \vec{u}(\vec{x}, t)$ and $P = P(\vec{x}, t)$, with $\vec{x}$ the position vector and t the time. With the aforementioned assumptions, the pressure-velocity Navier-Stokes equations are as follows:

$$\vec{\nabla} \cdot \vec{u} = 0, \tag{1}$$

$$\frac{\partial \vec{u}}{\partial t} + \left(\vec{u} \cdot \vec{\nabla}\right)\vec{u} = -\frac{1}{\rho}\vec{\nabla}P + \nu\Delta\vec{u}, \tag{2}$$

where Equation (1) stands for the continuity equation and Equation (2) stands for the momentum equation. In this formulation, spatial and temporal dependencies are omitted to enhance readability. The vorticity field ($\vec{\omega}$) is defined as

$$\vec{\omega} = \vec{\nabla} \times \vec{u}. \tag{3}$$

Taking the curl of Equation (2) leads to the Navier-Stokes equations in the velocity-vorticity formulation:

$$\vec{\nabla} \cdot \vec{u} = 0, \tag{4}$$

$$\frac{\partial \vec{\omega}}{\partial t} + \left(\vec{u} \cdot \vec{\nabla}\right)\vec{\omega} = \left(\vec{\omega} \cdot \vec{\nabla}\right)\vec{u} + \nu\Delta\vec{\omega}. \tag{5}$$

The Helmholtz decomposition of the velocity field is applied.[34] It leads to the definition of a scalar potential field (Φ) and a divergence-free vector potential field ($\vec{\Psi}$) such that

$$\vec{u} = \vec{\nabla}\Phi + \vec{\nabla} \times \vec{\Psi} = \vec{u}^{\Phi} + \vec{u}^{\Psi}. \tag{6}$$

- The potential velocity ($\vec{u}^{\Phi}$) contains the constant upstream velocity component ($\vec{u}^{\infty}$) ;
- The vorticity-induced velocity ($\vec{u}^{\Psi}$), or rotational velocity component, is the core of the method as it is generated by the vorticity-carrying particles.

A Poisson equation[35] is obtained by means of some vector calculus identities, the vorticity definition (Equation (3)), and the Helmholtz decomposition of the velocity field (Equation (6)). It reads

$$\Delta\vec{\Psi} = -\vec{\omega}. \tag{7}$$

Let G be the 3D Green's function such that

$$G\left(\vec{x}\right) = \frac{1}{4\pi\|\vec{x}\|}. \tag{8}$$

As reminded in Appendix A.1, the solution to Equation (7) is a convolution product, denoted $\star$, of G with $\vec{\omega}$:

$$\vec{\Psi}\left(\vec{x}, t\right) = G\left(\vec{x}\right) \star \vec{\omega}\left(\vec{x}, t\right) = \iiint_{\vec{y} \in \mathbb{R}^3} G\left(\vec{x} - \vec{y}\right)\vec{\omega}\left(\vec{y}, t\right)dv\left(\vec{y}\right), \tag{9}$$

with the volume of integration ($dv(\vec{y})$). The curl of Equation (9) is evaluated using Green's function (Equation (8)). It is assumed that all the hypothesis to invert partial derivatives and integrals are met. It is a common feature in continuous fluid dynamics. Hence, a formulation for the vorticity-induced velocity, also known as the Biot-Savart law, is obtained:

$$\vec{u}^{\Psi}\left(\vec{x}, t\right) = \vec{\nabla}_x \times \vec{\Psi}\left(\vec{x}, t\right) = \iiint_{\vec{y} \in \mathbb{R}^3} \vec{K}\left(\vec{x} - \vec{y}\right) \times \vec{\omega}\left(\vec{y}, t\right)dv\left(\vec{y}\right). \tag{10}$$

It is reminded that $\vec{y}$ is a constant with respect to the derivative variable that is $\vec{x}$ in Equation (10). This is specified by $\vec{\nabla}_x$ with a subscript. The Biot-Savart kernel ($\vec{K}$) is defined as

$$\vec{K}\left(\vec{x}\right) = \vec{\nabla}G\left(\vec{x}\right) = \frac{1}{4\pi}\vec{\nabla}\left(\frac{1}{\|\vec{x}\|}\right) = -\frac{1}{4\pi}\frac{\vec{x}}{\|\vec{x}\|^3}. \tag{11}$$

The kernel ($\vec{K}$) has a singular behaviour when $\|\vec{x}\| \to 0$. This issue is tackled using the regularized vortex particle method. To circumvent the singular behaviour of the kernel, regularized kernels have been developed and thoroughly studied in the literature.[17,18,27,33] As they are well documented, several regularized kernels ($\vec{K}_\varepsilon$) exist. The spatial smoothing parameter is denoted ε. The current implementation of the regularized kernels in Dorothy is either the Moore-Rosenhead (MR) kernel, of algebraic order 0:

$$\vec{K}_{\varepsilon,MR}\left(\vec{x}\right) = -\frac{1}{4\pi}\frac{\vec{x}}{\left(\|\vec{x}\|^2 + \varepsilon^2\right)^{3/2}}, \tag{12}$$

or the higher order Winckelmans-Leonard (WL) kernel, which is of algebraic order 2:

$$\vec{K}_{\varepsilon,WL}\left(\vec{x}\right) = -\frac{1}{4\pi}\frac{\left(\|\vec{x}\|^2 + \frac{5}{2}\varepsilon^2\right)\vec{x}}{\left(\|\vec{x}\|^2 + \varepsilon^2\right)^{5/2}}. \tag{13}$$

For the interested reader, the principle to develop regularized kernels is reminded in Appendix A.2.

2.2 | Discretized numerical approach: particle formalism

The whole fluid domain, denoted $\mathcal{D}$, is discretized into $N \in \mathbb{N}$ subparts called fluid particles or blobs. The i-th fluid particle is time-dependant and denoted $\mathcal{P}_i(t)$ meaning that $\mathcal{D} = \bigcup_{i=1}^{N}\mathcal{P}_i(t)$. The i-th fluid particle volume (Equation (14)), position (Equation (15)), and vorticity weight (Equation (16)), are defined as

$$V_i(t) = \iiint_{\mathcal{P}_i(t)} dv\left(\vec{x}\right), \tag{14}$$

$$\vec{X}_i(t) = \frac{\iiint_{\mathcal{P}_i(t)} \vec{x}\,dv\left(\vec{x}\right)}{\iiint_{\mathcal{P}_i(t)} dv\left(\vec{x}\right)} = \frac{\iiint_{\mathcal{P}_i(t)} \vec{x}\,dv\left(\vec{x}\right)}{V_i(t)}, \tag{15}$$

$$\vec{\Omega}_i(t) = \iiint_{\mathcal{P}_i(t)} \vec{\omega}\left(\vec{x},t\right)dv\left(\vec{x}\right) \simeq \vec{\omega}\left(\vec{X}_i(t),t\right)V_i(t). \tag{16}$$

The explanation of the similar or equal sign on the right side of Equation (16) comes from the assumption that the integral over the fluid particle domain can be approximated by the value of the function at the barycentre multiplied by the fluid particle volume. Following a similar process, the Biot-Savart law (Equation (10)) is written for the VP framework:

$$\vec{u}_\varepsilon^{\Psi}\left(\vec{x},t\right) = \sum_{j=1}^{N}\iiint_{\mathcal{P}_j(t)}\vec{K}_\varepsilon\left(\vec{x}-\vec{y}\right)\times\vec{\omega}\left(\vec{y},t\right)dv\left(\vec{y}\right) \simeq \sum_{j=1}^{N}\vec{K}_\varepsilon\left(\vec{x}-\vec{X}_j(t)\right)\times\vec{\Omega}_j(t). \tag{17}$$

The influence of the onset flow turbulence on vortex particles can be taken into account. The upstream turbulence velocity component ($\vec{u}'$) is modelled by means of the synthetic eddy method (SEM), initially developed by Jarrin et al,[36] and adapted in the VP framework.[28,29] Let $\vec{U}_i^{\Psi}(t) = \vec{u}_\varepsilon^{\Psi}\left(\vec{X}_i(t),t\right)$, $\vec{U}_i^{\Phi}(t) = \vec{u}_\varepsilon^{\Phi}\left(\vec{X}_i(t),t\right)$ and $\vec{U}_i(t) = \vec{u}\left(\vec{X}_i(t),t\right)$ define the i-th fluid particle velocity:

$$\vec{U}_i(t) = \vec{U}_i^{\Psi}(t) + \vec{U}_i^{\Phi}(t) + \vec{U}_i(t). \tag{18}$$

This last equation (Equation (18)) is the fundamental equation to evaluate the discrete velocity in Lagrangian VP methods, with $\vec{u}' = \vec{0}$ if the upstream turbulence is not modelled. A *treecode* algorithm is also implemented in Dorothy,[27] based upon the work of Lindsay and Krasny.[37] It aims at decreasing the computational cost of the vorticity induced velocity evaluation in Equation (18) with a user-defined error. This is based on a Taylor expansion of the regularized kernel and acts similarly to the fast multipole method (FMM).[38]

2.3 | Lagrangian vortex particle formulation of Navier-Stokes equations

The particle derivative (D/Dt) is defined by $\mathrm{D}/\mathrm{D}t = \partial/\partial t + (\vec{u} \cdot \vec{\nabla})$. The velocity-vorticity Navier-Stokes momentum equation (Equation (5)) is rewritten using the particle derivative. Moreover, two terms are added following literature[27,39] to account for a turbulent eddy viscosity ($\nu_T(\vec{x}, t)$), which enables the method to perform LES. Spatial and temporal dependencies of the right hand side terms are hidden to enhance readability.

$$\frac{\mathrm{D}\vec{\omega}}{\mathrm{D}t}\left(\vec{x}, t\right) = \underbrace{\left(\vec{\omega} \cdot \vec{\nabla}\right)\vec{u}}_{=\vec{S}(\vec{x}, t)} + \underbrace{(\nu + \nu_T)\Delta\vec{\omega} + \left(\vec{\nabla}\nu_T\right) \times \left(\Delta\vec{u}\right)}_{=\vec{L}(\vec{x}, t)} \tag{19}$$

- The stretching term is $\vec{S}(\vec{x}, t)$. This term can be expressed in three different formulations.[40,41] Nevertheless, once discretized, only the transposed formulation ensures the total vorticity conservation.[40,41] Consequently, this formulation has been chosen for all the computations carried out in this paper;
- The diffusion term, including turbulent diffusion, is $\vec{L}(\vec{x}, t)$. This term is handled via the particle strength exchange (PSE) method developed and detailed in previous studies.[42–45] This method allows to account for non-uniform viscous coefficients that may depend on position and time. In the presented computations, the turbulent viscosity ($\nu_T(\vec{x}, t)$) is evaluated either with Mansour's formulation[46] (Sections 4.1.2 and 4.2.2) or Smagorinsky's[47] (Section 4.3.3). The detailed implementation of the turbulent viscosity model in the Dorothy solver is available in Mycek.[27]

The Navier-Stokes momentum equation, lastly written in Equation (19), should be verified for all subparts of the domain and at all times. This is particularly true for each fluid particle. The integrated equation is obtained by integrating on the *i*-th fluid particle as follows:

$$\iiint_{\mathcal{P}_i(t)} \frac{\mathrm{D}\vec{\omega}}{\mathrm{D}t}\left(\vec{x}, t\right) \mathrm{dv}\left(\vec{x}\right) = \iiint_{\mathcal{P}_i(t)} \vec{S}\left(\vec{x}, t\right) \mathrm{dv}\left(\vec{x}\right) + \iiint_{\mathcal{P}_i(t)} \vec{L}\left(\vec{x}, t\right) \mathrm{dv}\left(\vec{x}\right). \tag{20}$$

The process leading from Equation (20) to Equation (22) is detailed in Appendix A.3. The numerical scheme is now complete, and the discretized Navier-Stokes set of equations is

$$\frac{\mathrm{d}\vec{X}_i}{\mathrm{d}t}(t) = \vec{U}_i(t), \tag{21}$$

$$\frac{\mathrm{d}\vec{\Omega}_i}{\mathrm{d}t}(t) = \vec{S}\left(\vec{X}_i(t), t\right) V_i(t) + \vec{L}\left(\vec{X}_i(t), t\right) V_i(t), \tag{22}$$

$$\frac{\mathrm{d}V_i}{\mathrm{d}t}(t) = 0, \tag{23}$$

where Equation (21) represents the discrete *i*-th particle advection with the fluid velocity (Equation (18)), Equation (22) the *i*-th particle vorticity evolution, and Equation (23) the *i*-th particle volume evolution. The particle volume evolution reduces to zero because of the mathematical aspects described in Appendix A.3. In the code, this Navier-Stokes set of equations can be integrated in time using either the second- or fourth-order Runge-Kutta time advancing schemes. The second-order Runge-Kutta is used for the computations presented in this work.

3 | LIFTING-LINE IN THE CONTEXT OF LAGRANGIAN VORTEX PARTICLE METHOD

Section 3 aims at explaining thoroughly the strategies developed to adapt the lifting-line filamentary viewpoint within the vortex particle formalism. Section 3.1 focuses on the geometrical descriptions and the flow analysis over the lifting profiles. Sections 3.2 and 3.3 represent the core of the present paper: the transcription of vortex filaments into particles together with the particles shedding. Eventually, Section 3.4 presents the remaining computational aspects with the space and time discretization as well as the computation of polar curves, when needed.

3.1 | Flow analysis and effect on lifting bodies

As a starting point, the different geometric axis systems to handle rotating blades are defined. It is worth mentioning that all the defined bases are direct and orthonormal. In the end, angular values are chosen to match the physical reality of the problem. First, the rotating base $(\vec{e}_x, \vec{e}_r, \vec{e}_\theta)$ is described with respect to the Cartesian system $(\vec{e}_x, \vec{e}_y, \vec{e}_z)$ as stated by the rotation matrix expressed in Equation (24). Vector $\vec{e}_r$ is the unitary vector aligned with the blade axis, which means that $\vec{e}_r$ is the lifting-line unitary vector. Second, another rotating base $(\vec{e}_{x\gamma}, \vec{e}_r, \vec{e}_\gamma)$, associated to the definition of each twist plus pitch angle (γ), is presented with Equation (25). Vector $\vec{e}_\gamma$ is aligned with the axis of the blade profile.

$$
\begin{pmatrix} \vec{e}_x \\ \vec{e}_r \\ \vec{e}_\theta \end{pmatrix} = \begin{pmatrix} 1 & 0 & 0 \\ 0 & \cos\theta & \sin\theta \\ 0 & -\sin\theta & \cos\theta \end{pmatrix} \begin{pmatrix} \vec{e}_x \\ \vec{e}_y \\ \vec{e}_z \end{pmatrix} = M_1(\theta) \begin{pmatrix} \vec{e}_x \\ \vec{e}_y \\ \vec{e}_z \end{pmatrix}
\tag{24}
$$

$$
\begin{pmatrix} \vec{e}_{x\gamma} \\ \vec{e}_r \\ \vec{e}_\gamma \end{pmatrix} = \begin{pmatrix} \cos\gamma & 0 & -\sin\gamma \\ 0 & 1 & 0 \\ \sin\gamma & 0 & \cos\gamma \end{pmatrix} \begin{pmatrix} \vec{e}_x \\ \vec{e}_r \\ \vec{e}_\theta \end{pmatrix} = M_2(\gamma) \begin{pmatrix} \vec{e}_x \\ \vec{e}_r \\ \vec{e}_\theta \end{pmatrix}
\tag{25}
$$

A blade profile is represented in Figure 1A, associated with its base $(\vec{e}_{x\gamma}, \vec{e}_r, \vec{e}_\gamma)$. The true velocity ($\vec{u}_t$), or relative velocity, is defined as the fluid velocity with respect to the blade profile reference frame. It is associated to the unitary vector $\vec{e}_\phi$ as depicted in Figure 1A,B. In the lifting-line model, it is assumed that the radial component of the true velocity is zero. So the true velocity can be decomposed as in Equation (26), in association with the ϕ angle defined in Equation (27):

$$
\vec{u}_t = u_t \vec{e}_\phi = u_t \sin(\phi)\vec{e}_x + u_t \cos(\phi)\vec{e}_\theta = u_x \vec{e}_x + u_\theta \vec{e}_\theta,
\tag{26}
$$

$$
\phi = \arccos\left(\frac{u_\theta}{u_t}\right).
\tag{27}
$$

Figure 1A represents the reference for projections definition because all the angles are defined in the $[0, +90]$ quarter. For instance, when considering a wind or tidal turbine facing an upstream velocity along $\vec{e}_x$, the pitch and twist angle $\gamma \in [-90°, 0°]$ is negative. The angle of attack (α) is defined using Figure 1A:

$$
\alpha = \gamma - (-\pi + \phi) = \pi + \gamma - \phi.
\tag{28}
$$

Equation (28) can also be obtained from Figure 1B by observing that $\pi = \phi + \alpha - \gamma$. The true velocity ($\vec{u}_t$) is evaluated using an adaptation of Helmholtz velocity decomposition (Equation (6)). This decomposition is specifically subdivided and adapted to the lifting-line configuration:
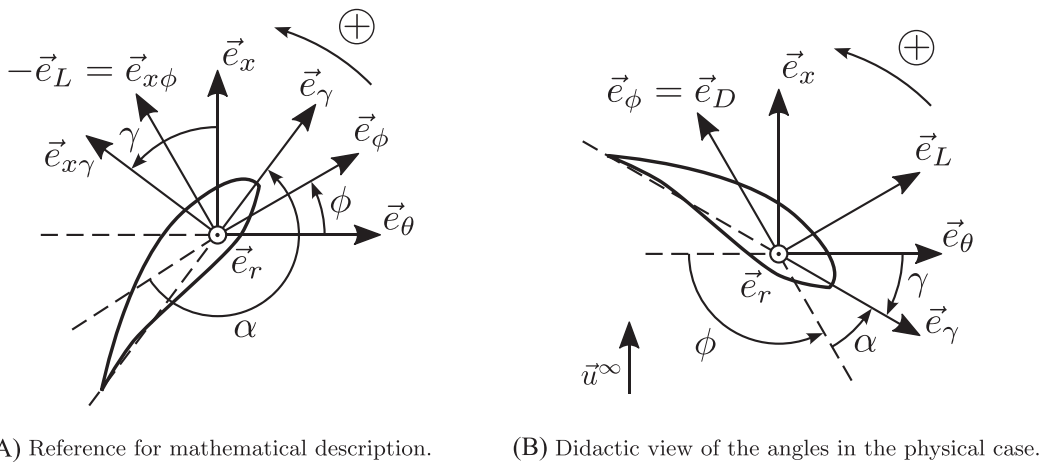

(A) Reference for mathematical description.   (B) Didactic view of the angles in the physical case.

FIGURE 1 Blade profile and true velocity with the associated bases. This allows the definition of the angle of attack (α).

$$\vec{u}_t = \vec{u}_m + \vec{u}^\infty + \vec{u}' + \underbrace{\vec{u}_{wake}^\Psi + \vec{u}_{near}^\Psi}_{=\vec{u}^\Psi}. \tag{29}$$

- $\vec{u}_m$ is the velocity generated by the self motion of the lifting body. In the present case, it is the local tangential velocity due to the blades rotation at angular velocity ω_{rot}. This means that $\vec{u}_m = -r\omega_{rot}\vec{e}_\theta$ with r the local radius;
- $\vec{u}^\infty$ is the mean upstream velocity and $\vec{u}'$ is the SEM-modelled upstream turbulence velocity component[28,29];
- $\vec{u}_{wake}^\Psi$ corresponds to the velocity induced by all the particles already shed and advected in the wake;
- $\vec{u}_{near}^\Psi$ corresponds to the velocity induced by the shed particles at the current time-step.

The present lifting-line method solves the flow using tabulated properties of the given lifting profile. This approach was initially described in[2,8]. This method is based on the Kutta-Joukowski theorem that links the action of the flow on a lifting body, which is the lift force ($\vec{L}_f$) by unit span length (dr), with the vorticity generation of the profile given by the bound circulation (Γ_B), positively oriented along $\vec{e}_r$. The Kutta-Joukowski theorem is given by Equation (30):

$$\frac{1}{\mathrm{d}r}\vec{L}_f = \rho\vec{u}_t \times \vec{\Gamma}_B = \rho u_t \Gamma_B\left(\vec{e}_\phi \times \vec{e}_r\right) = \rho u_t \Gamma_B \vec{e}_L, \tag{30}$$

where $\vec{e}_L$ is perpendicular to the direction $\vec{e}_\phi$ of the incoming true velocity ($\vec{u}_t$) as depicted in Figure 1B. The common lift force definition is reminded in Equation (31):

$$\frac{1}{\mathrm{d}r}\vec{L}_f = \frac{1}{2}\rho c u_t^2 C_L(\alpha)\vec{e}_L, \tag{31}$$

where C_L is the lift coefficient of the profile, function of the angle of attack (α), and c is the profile chord length. Injecting Equation (31) in Equation (30) allows to link directly the bound circulation with the tabulated lift coefficient:

$$\Gamma_B = \frac{1}{2}c u_t C_L(\alpha). \tag{32}$$

3.2 | Lifting-line coupling with vortex particle method

Modern lifting-lines are generally associated to Lagrangian vortex methods. But they are more frequently associated to panel or filament FVW implementations.[2-6] Nevertheless, despite core-spreading or other ad-hoc methods, FVW approaches prevent from the full account of diffusive aspects in the wake. The present vortex particle formulation, described in Section 2.3, takes into account all the diffusive aspects that enable to perform large eddy simulation (LES). Furthermore, the Lagrangian vortex particle method inherently enables turbines wake mixing and turbulence modelling in the upstream flow.[28,29] Therefore, the present approach is a solution to alleviate the FVW limitations and perform simulations on complex configurations. This is among the reasons why some lifting-line approaches within the Lagrangian vortex particle framework are currently being developed.[30-32] Those lifting-line associated with Lagrangian VP method, including the presented one, tend to merge the advantages of both approaches: the accuracy of shed vortices of the filament approach and the diffusive aspects of the particles. Eventually, to the authors opinion, the presented approach offers a new viewpoint on the transcription of the filamentary framework to the vortex particle one.

Figure 2 depicts this peculiar transcription from the filamentary framework towards the particle one. The upper part of the scheme in Figure 2 presents the shape of the blade with the dash-dotted black line. Various blade geometrical properties are specified: leading edge (LE), trailing edge (TE), the distance between the blade root and the rotation centre, or hub radius (R_h), and the blade length (L_b). The lifting-line is represented by the small-dotted black line located at 1/4 of the chord (c) behind the leading edge. $N_s \in \mathbb{N}$ is the number of sections in which the blade is divided. This defines the section width: d$r = L_b/N_s$. The lower part of the scheme in Figure 2 presents a zoom of the blade where a focus is made on three sections only. The vorticity panels carrying a bound circulation (Γ_B) are represented with the oriented filamentary contours. Hence, each panel is represented by four attached filaments. It is worth mentioning that these panels are represented in Figure 2 for the sake of explanation but they are not modelled in the numerical approach, only the particles are. Blade sections are numbered with their index $k \in [\![1,N_s]\!]$. Bound circulations are discretized following the blade sections. Hence, k index is also associated to the bound circulations ($\Gamma_B(k,t)$). Blade geometric properties (radii (r), pitch plus twist angles (γ), and chords (c)) are discretized with index $p \in [\![1,2N_s+1]\!]$. p index also refers to the true velocity ($\vec{u}_t$)
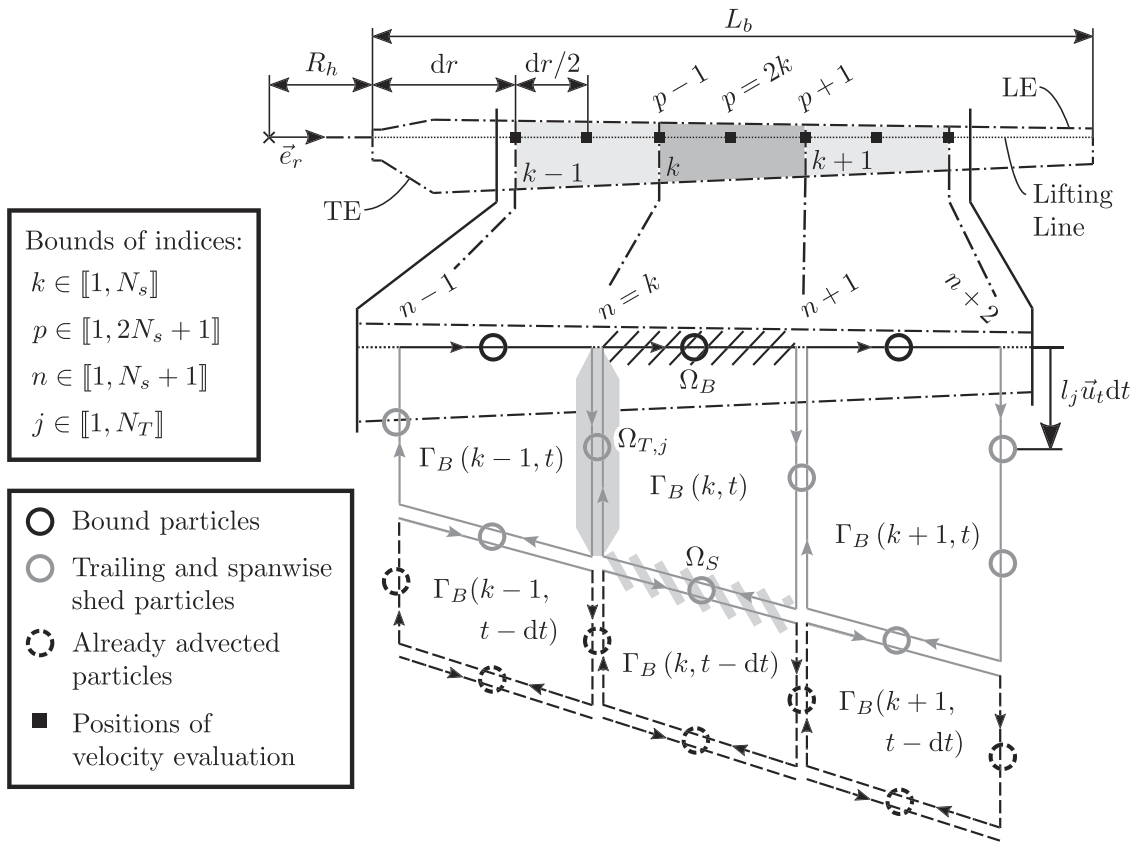
FIGURE 2 Schematic representation of the lifting-line associated to the VP method. The top part presents the lifting-line representation of the blade while the bottom part presents the particles shedding process. Black circles represent the bound particles $(\vec{X}_B, \vec{\Omega}_B)$. Grey circles, when associated to the filled grey area, represent the trailing shed particles at current time-step $(\vec{X}_{T,j}, \vec{\Omega}_{T,j})$. Grey circles, when associated to the hatched grey area, represent the spanwise shed particles at current time-step $(\vec{X}_S, \vec{\Omega}_S)$. The hatched black circles represent the already shed and advected particles in the wake $(\vec{X}_i, \vec{\Omega}_i)$. Each area represents the filaments that contribute to the vorticity of the associated type of particle.

as well as the associated ϕ and α angles. Both bound particles $(\vec{X}_B, \vec{\Omega}_B)$ and spanwise shed particles $(\vec{X}_S, \vec{\Omega}_S)$ are numbered with $k \in [\![1, N_s]\!]$ following Figure 2. Trailing filaments are numbered with $n \in [\![1, N_s + 1]\!]$. In the presented approach, there is naturally one more trailing filament than the number of blade sections, as depicted in Figure 2. Moreover, depending on the time-step, some trailing filaments can be multiple times longer than the blade section width (dr). Hence, as advised in literature[30,32] to discretize correctly the trailing filaments, the trailing shed particles are distributed along each trailing filament. The number of trailing shed particles along the n-th filament is evaluated as follows:

$$N_T = \max\left(1, \lfloor \vec{u}_t(p-1,t)dt / dr \rfloor\right),\tag{33}$$

with $\lfloor \rfloor$ being the floor function. Each trailing shed particle $(\vec{X}_{T,j}, \vec{\Omega}_{T,j})$ at a given trailing filament is denoted with subscript $j \in [\![1, N_T]\!]$.

The hatched black area represents the filament that influences the k-th bound particle vorticity weight $(\vec{\Omega}_B(k,t))$. The filled grey area represents the filamentary contributions that influence the j-th trailing shed particle vorticity weight $(\vec{\Omega}_{T,j}(n,t))$, as part of the n-th trailing filament. The hatched grey area represents the filaments that influence the k-th spanwise shed particle vorticity weight $(\vec{\Omega}_S(k,t))$. The thick-dotted black circles represent the particles that were already shed and advected in the wake at earlier time-steps $(\vec{X}_i, \vec{\Omega}_i)$. The thick-dotted black lines are the associated filaments.

The chosen boundary condition is that the bound circulation (Γ_B) is zero below the blade root and above the blade tip for all times (t). The bound circulation is set at zero for all k indices: $\Gamma_B(k, t = 0) = 0$ as initial condition.

3.3 | Particles shedding and loads evaluation

To deal with particles shedding process, the first objective is to assess the true velocity $(\vec{u}_t(p,t))$ using Equation (29). Evaluating the true velocity is necessary to compute as accurately as possible positions and vorticity weights of the trailing $(\vec{X}_{T,j}, \vec{\Omega}_{T,j})$ and spanwise $(\vec{X}_S, \vec{\Omega}_S)$ shed particles. Mean

upstream velocity ($\vec{u}^{\infty}$) and upstream turbulence ($\vec{u}'$) are immediately evaluated. As previously mentioned, the motion velocity is known for all p indexes: $\vec{u}_m(p,t) = -r(p)\omega_{rot}\vec{e}_\theta$. For all p indexes, the velocity ($\vec{u}_{wake}^{\Psi}(p,t)$) induced by all the particles advected in the wake ($\vec{X}_i, \vec{\Omega}$) is also known. It is evaluated by means of the Biot-Savart law (Equation (17)) with a treecode.[37] Then, the sum $\vec{u}^{\infty} + \vec{u}'(p,t) + \vec{u}_m(p,t) + \vec{u}_{wake}^{\Psi}(p,t)$ is known for a given position p and time t. This value is stored and serves as initialization for the true velocity. It remains to evaluate $\vec{u}_{near}^{\Psi}(p,t)$. This term represents the induction generated by the trailing ($\vec{X}_{T,j}, \vec{\Omega}_{T,j}$) and spanwise shed particles ($\vec{X}_S, \vec{\Omega}_S$) at the current time t. This velocity is also evaluated using the Biot-Savart law (Equation (17)) only with those shed particles. As $\vec{u}_{near}^{\Psi}(p,t)$ values impact the true velocities ($\vec{u}_t(p,t)$), the bound circulations ($\Gamma_B(k,t)$), associated to the first row of contours-oriented panels, are also changed. This, in turns, modifies the vorticity weight of the trailing ($\vec{X}_{T,j}, \vec{\Omega}_{T,j}$) and spanwise shed particles ($\vec{X}_S, \vec{\Omega}_S$). This highlights the need for a sub-iteration algorithm giving both accurate true velocities and vorticity weights for the trailing and spanwise shed particles. The sub-iteration algorithm is based on the fixed-point algorithm presented for FVW codes by van Garrel.[2] The complete algorithm in the context of vortex particle method is detailed in Appendix B.1. One of the key aspects in the presented approach is the definition of trailing and spanwise particles shedding positions (Equations (36) and (38)) and vorticity weights (Equations (37) and (40)). The present paper offers a different approach from previous studies[30–32] on this specific matter.

3.3.1 | Bound particles

First the k-th bound particle is considered. The bound particle is located at the middle of each filament ($dr\vec{e}_r$). Its position is defined by:

$$\vec{X}_B(k,t) = (k-0.5)dr\vec{e}_r. \tag{34}$$

The black-hatched area represented in Figure 2 highlights the filamentary contributions to the vorticity weight of the k-th bound particle.

$$\vec{\Omega}_B(k,t) = \Gamma_B(k,t)dr\vec{e}_r. \tag{35}$$

3.3.2 | Trailing shed particles

Second, the n-th trailing filament is considered. As explained previously, N_T trailing shed particles represent the filament. Each j-th trailing shed particle is positioned at

$$\vec{X}_{T,j}(n,t) = \vec{X}_B(k,t) - \frac{1}{2}dr\vec{e}_r + l_j\vec{u}_t(p-1,t)dt, \tag{36}$$

with $l_j = (j-0.5)/N_T$, the coefficient that distributes the trailing shed particles along the filament. The filled grey area represented in Figure 2 highlights the n-th filamentary contributions to each of the N_T trailing shed particle. This allows to easily define the j-th trailing shed particle vorticity weight:

$$\vec{\Omega}_{T,j}(n,t) = \frac{1}{N_T}(\Gamma_B(k-1,t) - \Gamma_B(k,t))\vec{u}_t(p-1,t)dt. \tag{37}$$

3.3.3 | Spanwise shed particles

Finally, the k-th spanwise shed particle is studied. The spanwise shed particle is positioned at

$$\vec{X}_S(k,t) = \vec{X}_B(k,t) + \frac{1}{2}dr\vec{e}_r + \vec{u}_t(p+1,t)dt + \frac{1}{2}\vec{s}(k,t), \tag{38}$$

with the spanwise vector being defined as

$$\vec{s}(k,t) = -\vec{u}_t(p+1,t)\mathrm{d}t - \mathrm{d}r\vec{e}_r + \vec{u}_t(p-1,t)\mathrm{d}t. \tag{39}$$

The hatched grey area represented in Figure 2 highlights that the k-th spanwise shed particle vorticity weight results from two different contributions. The first contribution comes from the tail of the panel at time t and the second one comes from the head of the panel at time $t - \mathrm{d}t$. This viewpoint leads to Equation (40), in which the angular step is defined as $\mathrm{d}\theta = \omega_{rot}\mathrm{d}t$.

$$\vec{\Omega}_S(n,t) = \Gamma_B(k,t)\vec{s}(k,t) + \Gamma_B(k,t-\mathrm{d}t)\mathrm{d}r\left(M_1(\mathrm{d}\theta)\vec{e}_r\right) \tag{40}$$

3.3.4 | Loads evaluation

When convergence is obtained for all the shed particles, the shedding process is completed. This leads to loads evaluation. For a given blade section, lift is evaluated using Equation (41) and drag using Equation (42):

$$\vec{L}_{f,k}(t) = -\frac{1}{2}\rho c(p)u_t^2(p,t)C_L(\alpha(p,t))\mathrm{d}r\vec{e}_{x\phi}, \tag{41}$$

$$\vec{D}_{f,k}(t) = \frac{1}{2}\rho c(p)u_t^2(p,t)C_D(\alpha(p,t))\mathrm{d}r\vec{e}_{\phi}, \tag{42}$$

where both lift and drag coefficients are interpolated within the tabulated values contained in the polar curves of lift (C_L) and drag (C_D) coefficients. Note that no correction is added to the polar coefficients at this point. By using Equations (41) and (42) and the rotation matrix defined in Equation (25), forces along $\vec{e}_x$ and $\vec{e}_\theta$ are obtained:

$$\begin{pmatrix} F_{x,k}(t) \\ 0 \\ F_{\theta,k}(t) \end{pmatrix} = M_2^{-1}(\phi(p,t))\left(\vec{L}_{f,k}(t) + \vec{D}_{f,k}(t)\right) = M_2(-\phi(p,t))\left(\vec{L}_{f,k}(t) + \vec{D}_{f,k}(t)\right). \tag{43}$$

To correctly evaluate the loads, blade tip corrections may be needed because the present LL-VP method does not represent the tip vortices influence on the lifting-line as accurately as FVW codes. Such corrections are all the more needed when the blades are designed with a significant chord length at blade tip. Two different load corrections are implemented: Shen's one[48] and Wimshurst's one.[49] Loads evaluation can be done either with one of those corrections or no correction at all. If activated, the selected correction provides two normalized coefficients, C_x and C_θ, that modify the loads radial distributions. With no correction activated, $C_x = C_\theta = 1$. Torque (Q, Equation (44)) and thrust (T, Equation (45)) of the turbine at the current time (t) are assessed via

$$Q(t) = \sum_{k=1}^{N_s} C_\theta F_{\theta,k}(t)r(2k), \tag{44}$$

$$T(t) = \sum_{k=1}^{N_s} C_x F_{x,k}(t). \tag{45}$$

Finally, all the particles including the ones already in the wake as well as the shed ones are advected using Equations (21) to (23), as indicated at the end of Section 2. The bound particles $(\vec{X}_B, \vec{\Omega}_B)$ velocity contribution, which represents the lifting-line contribution, is taken into account in the wake processing. However those bound particles do not contribute to the stretching term and diffusion term of Equation (22). The complete algorithm of the lifting-line associated to the vortex particle method, including the while-loop of sub-iterations, is exhibited in the flowchart of Figure B1 in Appendix B. From now on, the approach described above is referred to as 'Dorothy LL-VP'.

3.4 | Additional numerical aspects of the presented method

3.4.1 | Spatial and temporal discretization

According to the spatial positions of shed particles described in Section 3.2, the inter-particle spacing dh is characterized as

$$dh \simeq dr. \qquad (46)$$

From this inter-particle spacing dh, the regularization parameter, or smoothing parameter, ε is evaluated as

$$\varepsilon = 1.5 \times dh. \qquad (47)$$

As in many Lagrangian vortex particle methods, a global redistribution algorithm is necessary to ensure an homogeneous particles distribution in the computational domain.[18,50] Such a redistribution algorithm is especially required to mitigate the distortion of the Lagrangian grid. The redistribution algorithm avoids particles concentration inhomogeneity. As a consequence, a redistribution algorithm using the interpolation function M'_4 is implemented in the Dorothy solver.[27] The principle is to create new particles on a Cartesian grid with a cell size of dh. Then, the vorticity carried by the former particles is redistributed on those new particles with the help of the interpolation function M'_4. The computation continues only with the new particles. The redistribution is applied every 5 to 100 time-steps depending on the computation needs. The redistribution is performed everywhere in the domain except in minimal cylindrical volumes around each lifting-line present in the domain. This is done to avoid disturbing the particles shedding process.

As prescribed in literature,[23–25] a Lagrangian interpretation of the Eulerian CFL condition is used to set the computation time-step dt.

$$dt \lesssim \frac{dh}{\max(\|\vec{u}\|)} \qquad (48)$$

with $\max(\|\vec{u}\|)$ being the maximum velocity encountered in the field. For fixed wing computations, a preliminary evaluation leads to replace $\max(\|\vec{u}\|)$ by $\|\vec{u}^\infty\|$. A check is performed at the end of the computation. If $\max(\|\vec{u}\|) \geq \|\vec{u}^\infty\|$, the time-step (d$t$) is evaluated again and the computation is repeated with the new dt. For rotary wing computations, different vortex particle studies[30–32] suggest that the time-step should be driven by the turbine angular velocity. To correctly capture the dynamic of the wake, all those studies agree that the rotary wing should move of a few degrees within the time-step. The angular step values used in the present paper are reported in Sections 4.2.2 and 4.3.3.

Finally, as prescribed in Ploumhans and Winckelmans,[50] the quality of the computation is assessed using the mesh Reynolds number and the time-stepping condition. According to Ploumhans and Winckelmans,[50] those quantities should be of the order of magnitude of 1 for high resolution computations. However, the presented LL-VP method leads to computations that are no equivalent to direct numerical simulation (DNS). Hence, for the computations presented in Section 4, the maximum of the mesh Reynolds number in the domain is recorded at each time-step. It is monitored throughout the computation to ensure it remains fairly constant.

3.4.2 | Polar curves computation

First, this subsection can be bypassed if the polar curves (C_L, C_D) are provided with the studied case. For instance, in the Mexnext-III case studied in Section 4.2.2, polar curves are directly provided. Nevertheless, in the opposite case, a polar curves dataset needs to be created. This was particularly the case for the three LOMC-IFREMER tidal turbine study described in Section 4.3.3.

The first step is getting the 2D geometry of the lifting profile. The NACA profiles geometry used in Section 4.3.3 are obtained from the code described in Carmichael.[51] Once the profile geometry is known, polar curves for angles of attack $\alpha \in [-\alpha_s, +\alpha_s]$ are obtained from XFoil software thoroughly described in previous studies.[52,53] The stall angle of attack of the considered profile is α_s. The transition to turbulence in the boundary layer is set, according to van Ingen,[54] as a function of the turbulence intensity in the upstream flow. For the considered wind and tidal turbines, the compressibility effects are neglected. Consequently the Mach number is set to zero $M = 0$ in XFoil. This is consistent with the incompressibility assumption in the Navier-Stokes equations as mentioned in Section 2.1. Polars are then extended on the full 360° range by means of Viterna's method.[55] The maximum drag coefficient $C_{D,max}$ needed for Viterna's method is chosen as the value for a 2D flat plate. $C_{D,max} \simeq 2$ according to section 3-16 in Hoerner.[56] Eventually, C_L from Viterna's formula is regularized around $-180°$ and $+180°$ with quadratic Lagrange interpolating polynomial. An example of polar curves resulting from this methodology is shown in Figure C1 of Appendix C.

4 | WIND AND TIDAL TURBINES APPLICATIONS

Section 4 aims at presenting the accuracy of the newly implemented method on cases of increasing complexity. First, in Section 4.1.2, an elliptic wing is studied to validate Dorothy LL-VP numerical results and assess its spatial convergence. Second, in Section 4.2.2, three reduced velocities of the Mexnext-III case are studied. Eventually, in Section 4.3.3, a three tidal turbines in interaction configuration is chosen to highlight wake mixing and to analyse the fluctuating loads perceived by a downstream turbine. This tidal case study is carried out as a way to bridge tidal and wind turbine fields.

4.1 | Dorothy LL-VP validation on the elliptic wing

The main purpose of this Section 4.1.2 is to evaluate the behaviour of the method described in Section 3 on an elliptic wing with a flat plate profile. This choice has been made because this elliptic wing has a known analytical solution.

No tip correction is applied for all the elliptic wing computations.

A focus on the convergence of the numerical results towards the analytical ones with an increasing level of discretization is made.

4.1.1 | Analytical study of the elliptic flat plate

The analytical expression of the lift coefficient (C_L) for small angles of attack (α) is reminded for a flat plate profile: $C_L(\alpha) = 2\pi \sin(\alpha) \simeq 2\pi\alpha$. This equation is obtained from the potential theory.[9] The main analytical results on the elliptic wing with a flat plate profile are reminded. This wing is built with an elliptic chord distribution:

$$c(r) = c_{max} \sqrt{1 - \left(\frac{2r}{L_b} - 1\right)^2}, \tag{49}$$

where the wing is of length L_b and $r \in [0, L_b]$ is the spatial variable along $\vec{e}_r$ axis. c_{max} is the chord at the wing centre. Consequently, according to Katz and Plotkin,[9] this wing experiences an elliptic circulation distribution over the wingspan defined by:

$$\Gamma_{B,theo}(r) = \Gamma_{B,max} \sqrt{1 - \left(\frac{2r}{L_b} - 1\right)^2}, \tag{50}$$

where $\Gamma_{B,max}$ is the circulation at the wing centre. With S the surface of the elliptic wing, the aspect ratio (AR) is defined as:

$$AR = \frac{L_b^2}{S} = \frac{L_b^2}{\pi \frac{c_{max} L_b}{4}} = \frac{4L_b}{\pi c_{max}}. \tag{51}$$

In this approach, C_L is modified by the finite aspect ratio of the wing and it is constant along the wingspan, as shown with Equation (52). The bound circulation at wing centre (Equation (53)) is obtained from the lift coefficient (Equation (52)). Again, the complete demonstration can be found in Katz and Plotkin.[9]

$$C_L = \frac{2\pi}{1 + \frac{2}{AR}} (\alpha_\infty - \alpha_{L0}) \tag{52}$$

$$\Gamma_{B,max} = \frac{2L_b \|\vec{u}^\infty\|}{1 + \frac{AR}{2}} (\alpha_\infty - \alpha_{L0}) \tag{53}$$

The geometric angle of attack related only to the upstream velocity ($\vec{u}^\infty$) is α_∞. It does not take into account the wake-generated induction velocity. The angle of attack of zero lift (α_{L0}) is defined such that $C_L(\alpha_{L0}) = 0$. For the flat plate profile, $\alpha_{L0} = 0$. Eventually, according to Katz and Plotkin,[9] the true angle of attack (α) takes into account the influence of the velocity downwash induced by the wake (w_i), respectively defined by Equation (55) and Equation (54). Both quantities are constant along the wingspan.

$$w_i = -\frac{\Gamma_{B,max}}{2L_b} \tag{54}$$

$$\alpha = \alpha_\infty - \frac{\Gamma_{B,max}}{2L_b \|\vec{u}^\infty\|} \tag{55}$$

4.1.2 | Comparison between numerical and analytical results on an elliptic flat plate wing

To reproduce the elliptic wing configuration studied by van Garrel,[2] the wing length is set to $L_b = 5$ m and the maximum chord is $c_{max} = 1$ m. The upstream velocity vector, expressed in the cartesian axis system $(\vec{e}_x, \vec{e}_y, \vec{e}_z)$ is $\vec{u}^\infty = (1,0,0.1)$ m·s^{-1}. Those numerical inputs for the analytical solutions give the following values:

- $C_L \simeq 0.477$ (Equation (52), Figure 3A);
- $\Gamma_{B,max} \simeq 0.24$ m^2·s^{-1} (Equation (53), Figure 3B);
- $w_i \simeq 0.024$ m·s^{-1} (Equation (54), Figure 3C);
- $\alpha \simeq 4.34°$ (Equation (55), Figure 3D).

Different wing discretization are tested to demonstrate the numerical convergence towards the analytical results: $N_s \in \{15,30,60,90\}$. Space and time discretizations are evaluated using Equations (46) and (48). The inter-particle spacing after each redistribution process is dh, as described in Section 3.4. The redistribution is applied each 30 time-steps. The total physical time of the simulation is t_{max}. It is chosen such that the wake length is at least 5 times longer than the wing span. This means a wake length of 25m and thus $t_{max} \geq 25$s. Air properties are the standard ones at 25 °C: a kinematic viscosity $\nu \simeq 15.6 \times 10^{-6}$ m^2·s^{-1} and a mass density $\rho \simeq 1.18$ kg·m^{-3}. Computations are performed using MR kernel (Equation (12)). The number of processors, or CPUs, used for the computation is n_{CPU}. The computational time is denoted t_{CPU}. Each simulation run on an Intel Core I5-11500H processor of a personal computer, split between 12 computational threads. Table 1 summarizes the simulation parameters for each level of discretization.

Figure 3 gathers all the quantities of interest that are flow-related. Figure 3A represents the radial distribution of lift coefficient (C_L). Figure 3B represents the radial distribution of bound circulation (Γ_B) over the wingspan. Figure 3C represents the radial distribution of induced velocity, or downwash, (w_i). Finally, Figure 3D represents the radial distribution of angle of attack (α). The radial distributions of C_L, w_i and α present similar variations along the wingspan for a given level of discretization. The numerical results rapidly tend to the analytical values when increasing the number of blade sections N_s. However, some discrepancies are observed when approaching the wing tips. To the authors understanding, this phenomenon must result from the combination of multiple factors. First, contrary to the analytical results, the presence of tip vortices at the wing tips surely affects induction. Second, Dorothy LL-VP seems to experience a smoothing effect due to the particle formalism compared to the FVW results presented in van Garrel.[2] Eventually, Dorothy LL-VP blade discretization is constant with a given dr value. However, the FVW codes that show less discrepancies in the tip area[2,6] rely on a 'cosine' panel distribution which generates a refined discretization at wing tips. One of the future developments of Dorothy LL-VP may be to introduce the 'cosine' wing discretization. The reader can easily notice that the elliptic bound circulation distributions (Figure 3A) show a good agreement between numerical and analytical results. As the bound circulation is not constant along the wingspan, it is more difficult to analyse the convergence of the numerical results towards the analytical solution. This is the reason why a specific Normalized Root Mean Square Error, denoted NRMSE, is defined in Equation (56):

$$NRMSE(\Gamma_{B,num}) = \frac{1}{\Gamma_{B,max}} \sqrt{\frac{\sum_{k=1}^{N_s}(\Gamma_{B,num}(k) - \Gamma_{B,theo}((k+0.5)dr))^2}{N_s}}. \tag{56}$$

It represents the integrated error between the numerically computed bound circulations ($\Gamma_{B,num}$), averaged on the last 10 iterations, and the analytical ones ($\Gamma_{B,theo}$) based on Equation (50). The normalizing factor chosen for this NRMSE is the analytical maximum bound circulation ($\Gamma_{B,max}$). For each level of discretization (N_s), the NRMSE is computed with Equation (56). It is multiplied by 100 to be analysed in percent. Figure 4A represents the decrease of this NRMSE with increasing level of discretizations. While the relative error is at 8% for 15 blade sections, it progressively decreases to around 2% for 90 blade sections. The rate of convergence is approximately $N_s^{-0.6}$. Eventually, Figure 4B represents the sub-iteration error e_{SI}, defined in Equation (B3) of Appendix B, versus the sub-iteration number n_{SI} on a log-log diagram. In Figure 4B, for a given level of discretization (N_s), each dot represents the mean of all the points at the considered sub-iteration index. Additionally, vertical lines are added to

TABLE 1 Elliptic wing cases computational parameters.

N_s (-)	15	30	60	90
dh (m)	0.33	0.17	0.08	0.056
dt (s)	0.33	0.16	0.08	0.055
t_{max} (s)	25	25	25	25
n_{CPU} (-)	12	12	12	12
t_{CPU} (hh:mm:ss)	00 : 00 : 03	00 : 01 : 04	00 : 23 : 54	01 : 49 : 50

(A) Lift coefficient C_L.

(B) Bound circulation Γ_B.

(C) Downwash w_i.
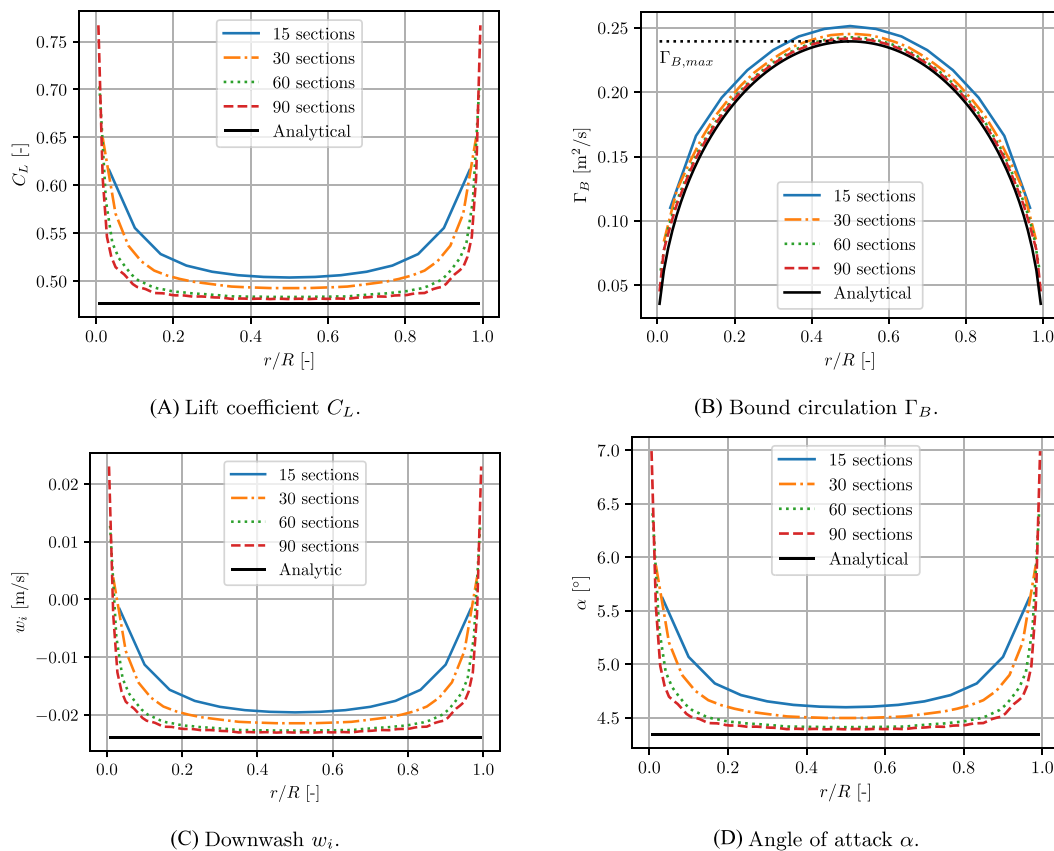
(D) Angle of attack α.

FIGURE 3 Elliptic wing radial distributions of lift coefficient, bound circulation, downwash and angle of attack.

represent the associated standard deviations. However, those standard deviations are of small magnitude. Hence, they are most of the time masked by the markers in Figure 4B. The rate of decrease of the sub-iteration error is approximately n_{SI}^{-3}.

Lastly, Figure 5 represents a didactic view of the particles together with the elliptic wing. The fluid particles are represented at their positions ($\vec{X_i}$) with a normalized colour scale representing their vorticity weight magnitude ($\vec{\Omega}$). Contrary to the results shown in Table 1, no redistribution is performed on the computation shown in Figure 5. This choice was made to enhance readability of the obtained figure. With the help of the vorticity weight colours, the two tip vortices can easily be noticed in the wake. The core of these two tip vortices can be identified by the yellow coloured particles issuing from each blade tip. The farthest those particles are from the wing, the more they lose their intensity while they drag other vortex particles to rotate around them. Moreover, the start up vortex can also be identified. This vortex faces the wing in the spanwise direction. It is linked to the vortex particles shed at the very first time-step. It can be interpreted as a direct consequence of Kelvin's theorem of circulation.[9] Its presence is a sign that the code behaves properly. Computation results presented in Figure 5 come from Dorothy LL-VP, so the wing representation is 1D as stated in Section 3. Nevertheless, as a matter of visual understanding, a 2D surface wing is rebuilt using the chord distribution. The normalized colourization of the wing represents the distribution of bound circulation over the wingspan, averaged over the last 10 iterations.
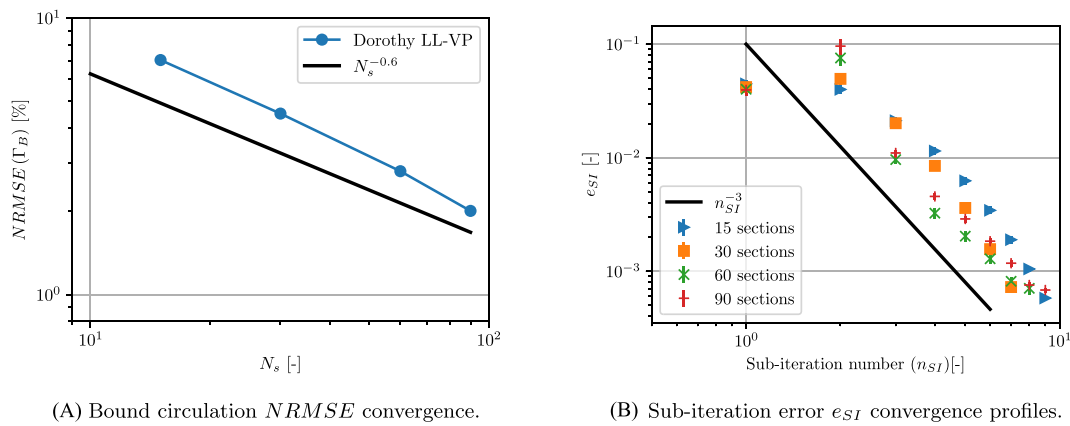
(A) Bound circulation $NRMSE$ convergence.

(B) Sub-iteration error e_{SI} convergence profiles.

FIGURE 4 Focus on bound circulation convergence and sub-iteration error profiles.
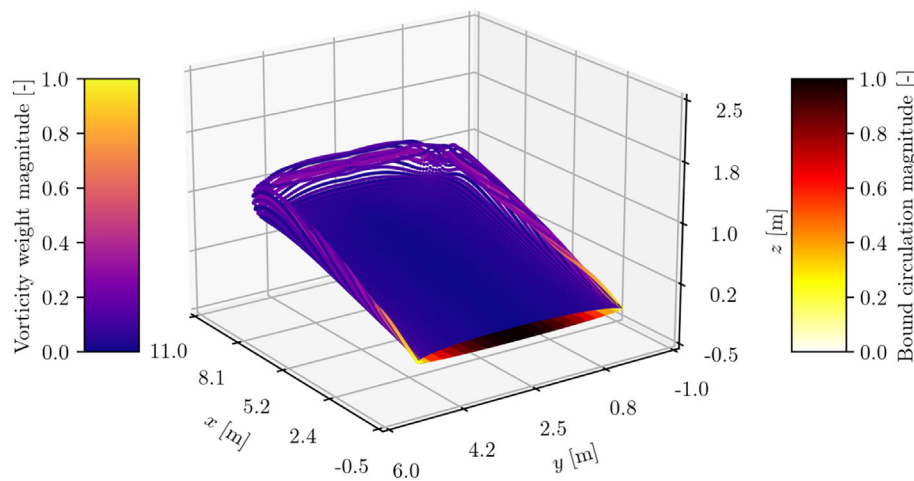

FIGURE 5 Visualization of an elliptic wing computation with 90 sections at $t \simeq 11$s. The 2D elliptic wing is built afterwards by the visualization tool. No redistribution is performed to ease the readability.

In conclusion, Dorothy LL-VP results proved to have a good accuracy on this elliptic wing configuration. The present implementation proved to converge towards the analytical solution for an increasing level of discretization. As a result of the sensitivity analysis on the blade discretization, different strategies can be chosen. A blade discretization around 20 sections will result in mid-fidelity computations that mitigate the computational cost. On the contrary, a level of discretization of 40 sections or more results in highly detailed computations with a significant computational cost.

4.2 | Wind turbine analysis: Mexnext-III study

The Mexnext-III Technology Collaboration Program (TCP) has been conducted under the leadership of the International Energy Agency (IEA) from 2015 to 2017. This program focused in particular on the analysis of the dataset produced during a measurement campaign of the New MEXICO 4.5 m rotor, conducted in 2014 at the German Dutch wind tunnel DNW. The experiments on steady upstream flow conditions have been run for three reduced velocities: one in stall region, one near optimum power coefficient and one in overspeed region. The Mexnext-III program aimed at enhancing and validating aerodynamic modelling tools through the investigation of the processed experimental data. It is crucial to validate aerodynamic tools not only on integrated quantities such as power and thrust coefficients, but also on radial distribution of loads and on wakes near the rotor which help to understand complex aerodynamic behaviours. Mexnext-III gathered numerous state-of-the-art aerodynamic modelling codes to create a benchmark comparison with the experimental results. In view of benchmarking and validating the present numerical implementation, the three Mexnext-III configurations are presented here.

4.2.1 | Simulations parameters and overview

First, Table 2 provides an overview of the computational parameters used in Dorothy LL-VP to run the Mexnext-III cases. It gathers information that are shared by all the cases. The pieces of information reported in Table 2 are available in Schepers et al.[57] The number of sections for each blade (N_s) and the associated spatial discretization after redistribution (dh, Equation (46)) are specified in Table 2. As stated in the conclusion of Section 4.1.2, the choice of $N_s = 40$ is a compromise between high quality results and a reasonable computational cost. The Wimshurst's tip correction on loads[49] is applied on all Dorothy LL-VP Mexnext-III results. See Section 3.3 for Wimshurst's loads tip correction implementation details. Note that the pitch angle sign given in Table 2 is opposed to the one presented in Schepers et al.[57] This is due to the sign convention chosen for the angles. See Section 3.1, and specifically Figure 1, for the mathematical definition of the present approach.

The case-specific parameters are reported in Table 3 for each studied reduced velocity, or tip speed ratio. The tip speed ratio (TSR) is defined as:

$$TSR = \frac{(R_h + L_b)\omega_{rot}}{\|\vec{u}^\infty\|}. \tag{57}$$

The mean upstream flow velocity ($u^\infty = \|\vec{u}^\infty\|$) and fluid density ($\rho$) relate to the specific upstream flow conditions in which have been operated the New MEXICO rotor during the experiments. Note that the change of TSR between the cases is not due to a change of angular velocity but to a change of mean upstream flow velocity. The chosen time-step (dt) following specifications of Section 3.4, together with the associated angular step (dθ), are given. Redistribution is performed every 50 time-steps. Following,[58] 99% of the axial induction is taken into account with a wake longer than 3.5 times the rotor diameter (D). Hence, the total physical time (t_{max}) is set for each case, depending on the mean upstream velocity, such that the wake expansion is more than $3.5D$. This ensures to reach a steady velocity induction providing converged near wake flow and converged blade loads. Eventually, for each computation to run on Intel Broadwell EP nodes, the number of CPUs (n_{CPU}) as well as the computational time (t_{CPU}) are specified. It can be noticed that the computational time for cases 2 and 3 starts being costly. In that respect, a deep work to enhance Dorothy LL-VP optimization and parallelization has already started.

Similarly to Figure 5 for the elliptic wing, Figure 6 is a didactic representation of Dorothy LL-VP computation of Mexnext-III case 1, low TSR, with 40 blade sections. No particles redistribution is performed here so that specific structures can be identified in the wake. The fluid particles are represented at their positions ($\vec{X}_i$) with a normalized colour scale representing their vorticity weights ($\vec{\Omega}_i$). Blade tip vortices can be identified by noticing the yellow vortex particles in the wake issuing from blade tips. This yellow colour shows the strong vorticity carried by those particles. The wake consists in three helical layers of vortex particles that follow their associated blade rotation. Figure 6 visualization comes from Dorothy LL-VP, so the three blades representation is 1D. Nevertheless, as a matter of visual understanding, 2D surface blades are built on top of the simulation results using the original chord and pitch plus twist distributions. The normalized colourization of the wing is built upon the distribution of the norm of the net aerodynamic force $\|\vec{L}_{f,k} + \vec{D}_{f,k}\|$ over the wingspan.

4.2.2 | Mexnext-III results analysis

The first objective of this subsection is to assess Dorothy LL-VP loads and performance results accuracy in comparison with some state-of-the-art codes. Among all the results presented in Schepers et al,[57] the ones from IFPEN VL and ECN Aero AWSM (filamentary FVW codes), and DTU AL (CFD actuator-line method) serve as the numerical benchmark. This choice is made because those methods present a proximity to the current

TABLE 2 Common parameters for all three Mexnext-III studied cases.

R_h (m)	L_b (m)	N_s (-)	dh (m)	Pitch angle (°)	ω_{rot} (rad·s⁻¹)	ν (m²·s⁻¹)
0.21	2.04	40	0.051	+2.3	44.5	15.3×10^{-6}

TABLE 3 Specific parameters for each Mexnext-III studied case.

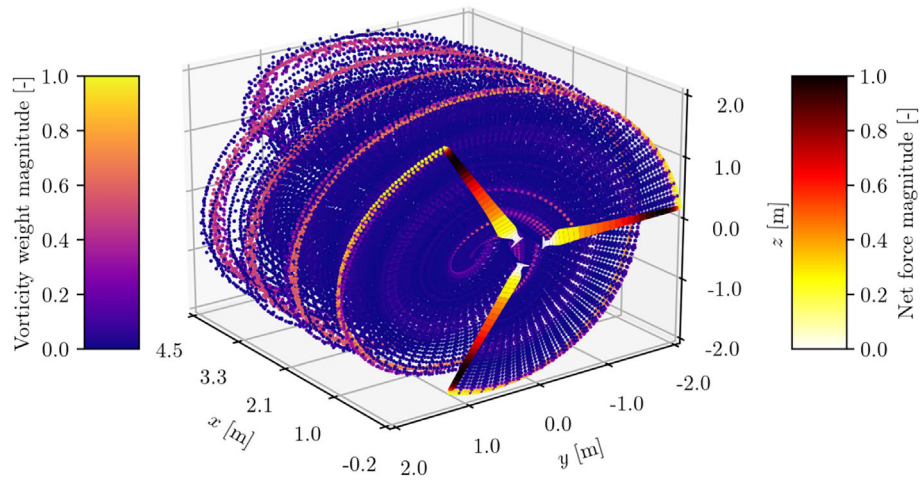| Case	TSR	u^∞ (m·s⁻¹)	ρ (kg·m⁻³)	dt (s)	dθ (°)	t_{max} (s)	n_{CPU} (-)	t_{CPU} (hh:mm:ss)
1	4.2	24.05	1.195	2.0×10^{-3}	5.1	1.0	140	09 : 16 : 46
2	6.7	15.06	1.191	1.7×10^{-3}	4.3	1.5	140	32 : 06 : 42
3	10	10.05	1.197	1.2×10^{-3}	3.1	1.8	140	42 : 28 : 25

FIGURE 6 Visualization of a Mexnext-III simulation of case 1, low *TSR*. The 2D blades of New MEXICO rotor are built afterwards by the visualization tool. No redistribution is performed.
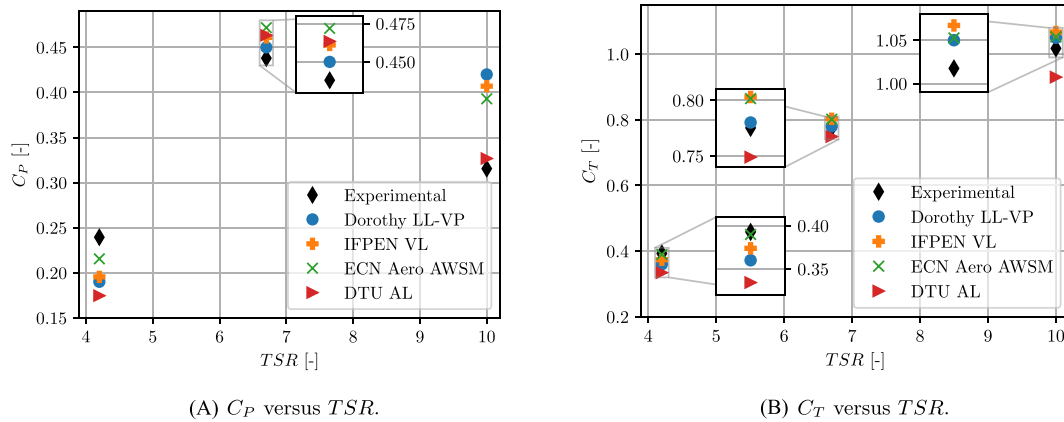

(A) C_P versus TSR.

(B) C_T versus TSR.

FIGURE 7 Mexnext-III performance comparison as a function of *TSR* including numerical and experimental results.

(A) Case 1, $TSR = 4.2$.
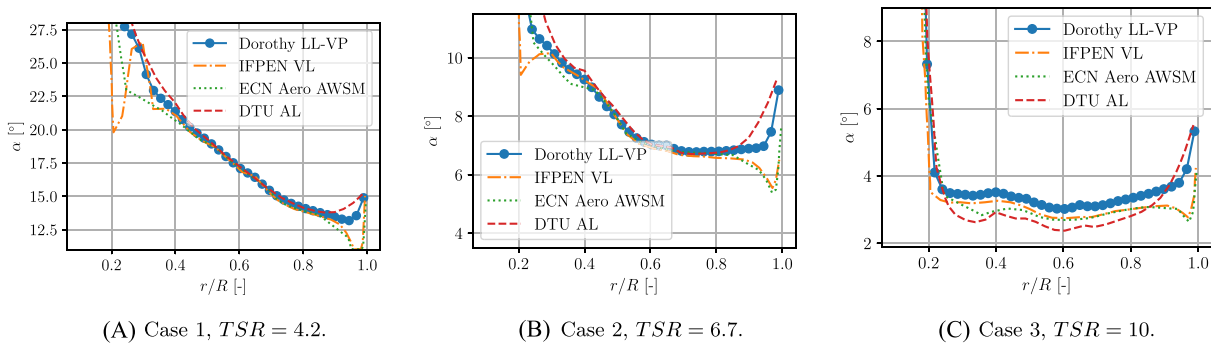
(B) Case 2, $TSR = 6.7$.

(C) Case 3, $TSR = 10$.

FIGURE 8 Radial distribution of angles of attack (α) for all Mexnext-III cases.

numerical approach. The turbine torque (Q) and thrust (T) are studied. On the one hand, they are studied through their normalized version: power (C_P) and thrust (C_T) coefficients, as presented in Figure 7. On the other hand, those performance results are related with the radial angle of attack (Figure 8) and loads distributions (Figure 9). The spatial parameter of those radial distributions is divided by $R = R_h + L_b$. The comparison is made between results obtained with Dorothy LL-VP, experiments, and other state-of-the-art codes. Power (C_P, Equation (58)) and thrust (C_T, Equation (59)) coefficients are defined as
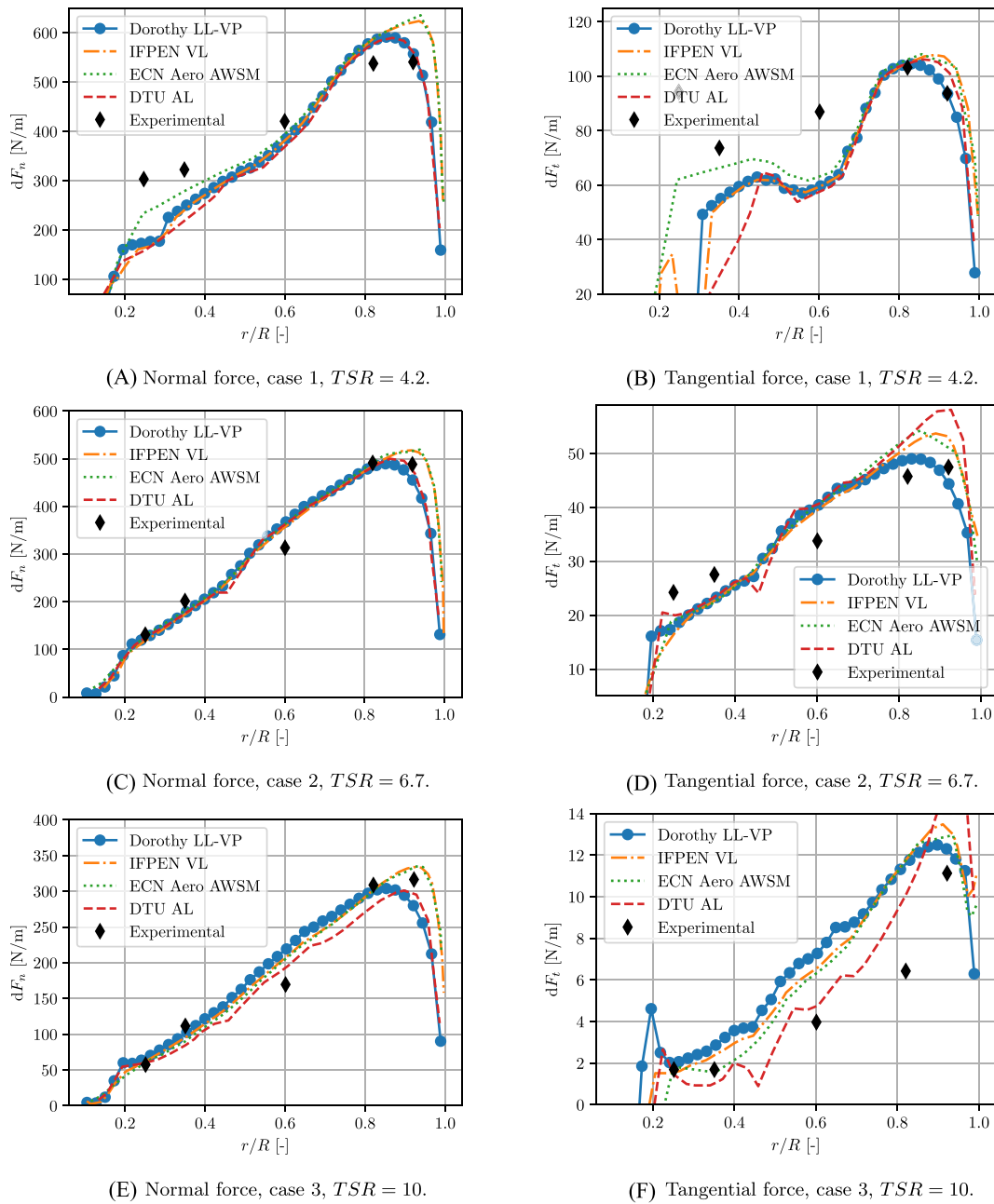
(A) Normal force, case 1, $TSR = 4.2$.

(B) Tangential force, case 1, $TSR = 4.2$.

(C) Normal force, case 2, $TSR = 6.7$.

(D) Tangential force, case 2, $TSR = 6.7$.

(E) Normal force, case 3, $TSR = 10$.

(F) Tangential force, case 3, $TSR = 10$.

FIGURE 9 Radial distribution of blade loads for all three Mexnext-III cases.

$$C_P = \frac{\omega_{rot} Q}{\frac{1}{2}\rho\pi(L_b + R_h)^2 \|\vec{u}^\infty\|^3}, \tag{58}$$

$$C_T = \frac{T}{\frac{1}{2}\rho\pi(L_b + R_h)^2 \|\vec{u}^\infty\|^2}. \tag{59}$$

It is worth mentioning that Mexnext-III torque (Q) and thrust (T) are not computed using Equations (44) and (45) respectively. In fact, and to be consistent with the experiment, torque and thrust evaluation is done through a linear combination of the numerical loads evaluated at some specific radial positions, where the experimental blade loads were measured. The methodology and set of linear combination coefficients are provided in Schepers et al.[57] All Dorothy LL-VP results are averaged over the last 50 iterations for each case.

Concerning the stall or low *TSR* region (case 1), all the codes are in good agreement with the experimental results, mainly for C_T. This is all the more interesting that a significant part of the blade, mainly close to the root, experiences a separated flow for this case according to literature.[59,60]

This is linked to the high angles of attack in this blade region predicted by all the codes, see Figure 8A. However, the various numerical methods present loads distributions that can vary significantly near the blade root, see Figure 9A,B. This phenomenon echoes the separated flow observed in blade resolved CFD studies.[59,60] This highlights that the stall region loads distributions are difficult to represent with polar curve based methods. But the introduced error seems to be averaged when looking at integrated quantities as the power and thrust coefficients have been evaluated accurately by all the codes. Finally, a focus is done on the angle of attack distributions of this low TSR case (Figure 8A). It is noticed that the vortex particle representation of the fluid in Dorothy LL-VP smoothes the tip vortex influence on the angle of attack results when comparing to IFPEN VL and ECN Aero AWSM (FVW codes). Some in-house tests were conducted to transform the first row of particles, that is to say the trailing and spanwise shed particles at time t, into filaments, only in the velocity evaluation of the sub-iteration process. This means that only the component $\vec{u}_{near}^{\psi}$, see Section 3.3, was affected by this change. The obtained angle of attack distribution for Dorothy LL-VP was very close to the ones of the FVW codes presented here. Hence, to the authors opinion, the vorticity that is shed at the current time t is interpreted as the wake part that drives this tip vortex influence upon the blade. However, this approach was finally not kept because it resulted in an unstable sub-iteration process which could diverge in an unpredictable manner. This was judged to be not acceptable as a stable code is a necessity. Nevertheless, looking in such a direction for further improvements could be a possibility as hybrid FVW-VP methods are being developed.[32]

In the optimum power coefficient region, Mexnext-III case 2, all the codes, including Dorothy LL-VP, tend to slightly overestimate the turbine C_P compared to the experimental results. Nevertheless, numerical and experimental results on C_T are very consistent at this TSR. Both the angle of attack distributions, see Figure 8B, and the loads distributions, see Figure 9C,D, are globally consistent for all the numerical methods. As previously mentioned, the tip region of the angle of attack distribution of the Dorothy LL-VP method shows that the tip vortex influence on the lifting-line is smoothed compared to FVW codes: IFPEN VL and ECN Aero AWSM. This results in slightly higher angles of attack at blade tip for Dorothy LL-VP compared to FVW codes. In this blade region, small changes in the angles of attack leads to significant loads and performance differences. If Whimshurst's tip loads correction was disabled, Dorothy LL-VP angles of attack would remain the same as the one shown in Figure 8B, but the loads near the blade tip would be extremely high, leading to incorrect performance evaluation. This observation explains why the authors chose to apply such a tip loads correction. It is still unclear whether adapting a 'cosine' blade discretization into Dorothy LL-VP framework would result in an enhancement of the tip vortex influence on the angles of attack distribution.

Finally, in the overspeed region, Mexnext-III case 3, two groups of results can be identified concerning the C_P. Contrary to DTU AL and the experimental results that evaluate the power coefficient near 0.32, Dorothy LL-VP and the FVW codes evaluate the C_P higher, around 0.4. As previously observed, the thrust coefficient C_T evaluations from all the codes are in good agreement with the experimental result. Both the angle of attack distributions, see Figure 8C, and the loads distributions, see Figure 9E,F, present the same variations for all the numerical methods. However one can notice that the DTU AL angle of attack distribution is slightly lower on a major part of the blade compared to the other numerical methods, see Figure 9F. This explains why DTU AL tangential load distribution is lower than all the other numerical methods at this TSR, see Figure 9F. The tangential load distribution of DTU AL results is very close to the experimental ones. This explains why this method predicts a power coefficient closer to the experimental results than the other numerical methods at this TSR. In the angle of attack distributions, see Figure 8C, it is noticed again that Dorothy LL-VP method does not reproduces accurately the tip vortex influence compared to the FVW methods: IFPEN VL and ECN Aero AWSM.

The second objective of this subsection is to assess Dorothy LL-VP wake evaluation near the rotor. The Mexnext-III case 2, which is the case of the TSR of the turbine optimum performance, is thoroughly studied. Dorothy LL-VP results are plotted against the Mexnext-III experimental data and the IFPEN VL numerical results. The experimental data comes from the PIV measurements done at the German Dutch wind tunnel and described in Schepers et al.[57] The IFPEN VL (FVW code) data have been initially published in Blondel et al.[61] The resulting velocity profiles are presented in Figure 10. Note that D represents the turbine diameter. Two different velocity profiles are studied to achieve the present comparison. The first one is an axial profile starting at the position $(-4.5, 1.5, 0.0)$ and ending at $(6.0, 1.5, 0.0)$, in metres in the Cartesian reference frame centred at the turbine rotation centre. The velocity record is instantaneous in this axial velocity profile. A blade has to be positioned on the vertical axis, along $\vec{e}_z$, to record this velocity profile. The three velocity components (u_x, u_y, u_z) from this axial velocity profile are respectively presented in Figure 10A,C,E. A good agreement between Dorothy LL-VP results and numerical results from IFPEN VL as well as experimental results is observed. The single noticeable aspect is a little discrepancy in Dorothy LL-VP results on u_y (Figure 10C) and u_z (Figure 10E) around $x \simeq 1D$ compared to IFPEN VL results. In spite of this element, the global trends for all the velocity components of this instantaneous velocity profile are very similar between Dorothy LL-VP and IFPEN VL numerical results and the experimental results. The second velocity profile is radial. It is located behind the rotor starting at the position $(0.3, 0.3, 2.8)$ and ending at $(0.3, 2.8, 0.0)$, in metres in the Cartesian reference frame centred at the turbine rotation. The velocity record of this radial velocity profile is averaged on $110°$ with a blade starting in the vertical position. The three averaged velocity components (u_x, u_y, u_z) for this radial velocity profile are respectively presented in Figure 10B,D,F. A very good agreement is observed between Dorothy LL-VP and IFPEN VL numerical results on all the velocity components. Both numerical result shows a reasonable similarity with experimental results except for the u_y velocity component that appears to be numerically underestimated.
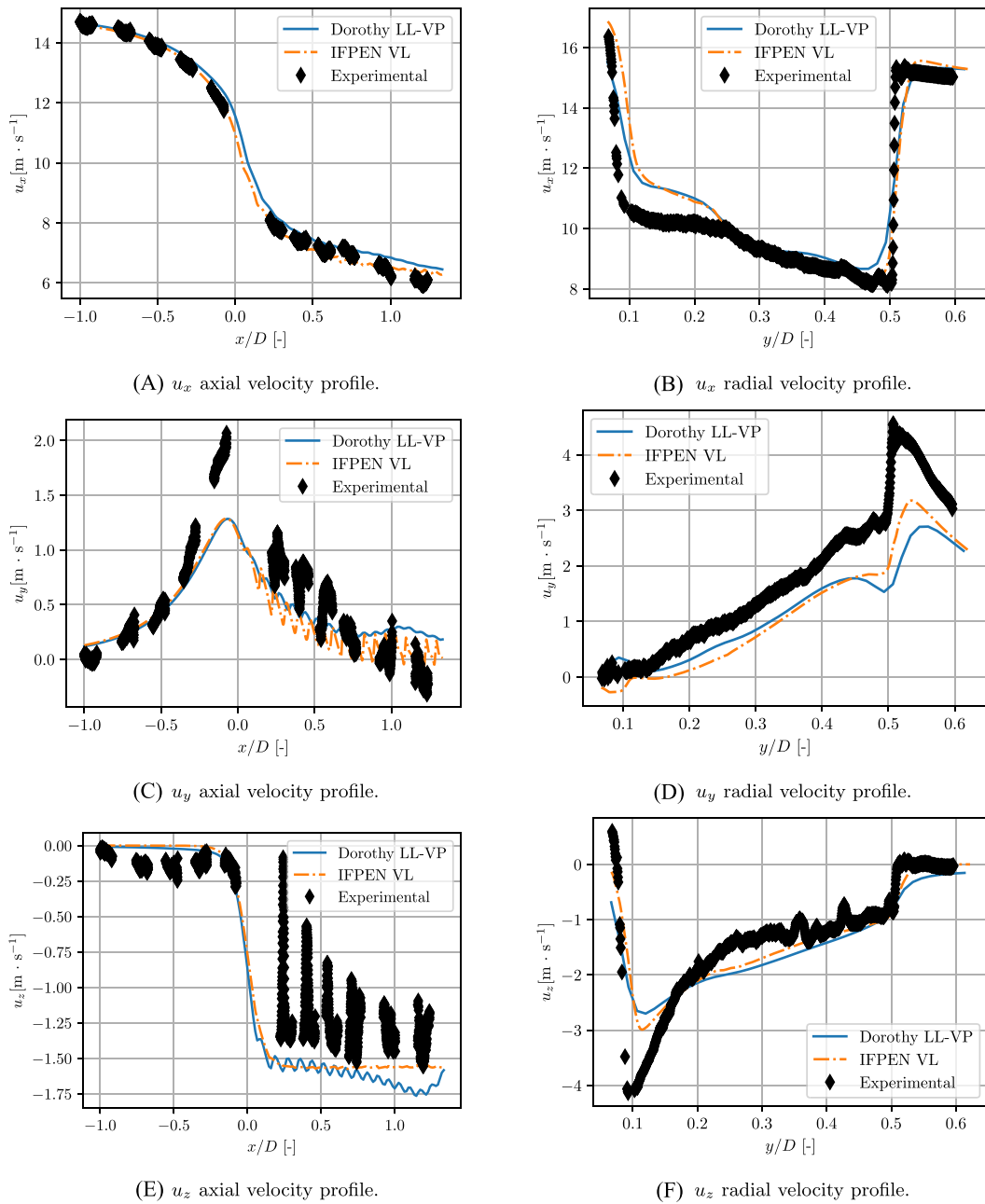
(A) u_x axial velocity profile.

(B) u_x radial velocity profile.

(C) u_y axial velocity profile.

(D) u_y radial velocity profile.

(E) u_z axial velocity profile.

(F) u_z radial velocity profile.

FIGURE 10 Axial and radial velocity profiles for Mexnext-III case 2, medium *TSR*.

4.3 | Three tidal turbines with wake mixing

After having demonstrated the capabilities of the LL-VP method for a single wind turbine, the objective of this Section 4.3.3 is to highlight the ability of this method to accurately simulate complex wake interaction situations for multiple tidal turbines. To the author's viewpoint, this proves the purpose of such a lifting-line associated to a vortex particle method. Not only the code is able to give accurate loads but it also computes wake interaction with its consequences on the downstream turbines blade loads. After presenting the set-up specifications of a three turbines array case, the results in term of wake dynamic and in term of performance and loads are studied in order to highlight the ability of the method to reproduce the turbines interaction effects.

4.3.1 | Set-up specifications

The present case reproduces one of the configurations coming from an experimental campaign previously conducted in the IFREMER wave and current flume tank.[62] The thorough analysis of this three-turbine experiment is detailed in Gaurier et al.[63] The geometrical configuration of the turbines positioning is described in Figure 11A. As in Gaurier et al,[62] the tidal turbine geometry is the scaled LOMC-IFREMER model. Compared to the geometry originally published in Mycek et al,[64] a global pitch of approximately 4.87° is applied such that the pitch plus twist angle (γ) is zero at blade tip. LOMC-IFREMER tidal turbine blade geometry is specified in Table C1 of Appendix C. In the computations, each blade is divided in 25 sections to mitigate the computational cost. General blade properties are reported in Table 4.

The mean upstream flow properties are set to match the experimental ones. This is the reason why the velocity average (u^∞) as well as standard deviations ($\sigma_{u_x}, \sigma_{u_y}, \sigma_{u_z}$) and turbulence integral length scale (L_I) have been directly computed on the experimental database available in Gaurier et al.[62] at 1D upstream of the two upstream turbines. The resulting 3D turbulence intensity is 2.0% when computed as follow:

$$TI_{3D} = \sqrt{\frac{\sigma_{u_x}^2 + \sigma_{u_y}^2 + \sigma_{u_z}^2}{3\left(\overline{u_x}^2 + \overline{u_y}^2 + \overline{u_z}^2\right)}}, \tag{60}$$

with $\overline{q}$ denoting the time average of a given quantity q. As mentioned in Section 2.1, the upstream turbulence is reproduced in Dorothy LL-VP using the synthetic eddy method initially developed in Jarrin et al[36] and following the specific implementation of Choma Bex et al.[29] At the end of the computation, upstream turbulence intensity and integral length scale are checked to ensure they match the experimental upstream conditions detailed in Table 5. The water properties used for the computations are the ones considered at standard temperature and pressure. Those flow properties are summarized in Table 5.

Polar curves for each profile are computed with the methodology explained in Section 3.4.2. An approximate local Reynolds number is computed at 70% of the blade following Equation (61):

$$Re_{70} = \frac{c_{70}\sqrt{(u^\infty)^2 + (R_h + 0.7 \cdot L_b)^2 \omega_{rot}^2}}{\nu}. \tag{61}$$

c_{70} represents the local chord at 70% of the blade. For the considered case, the obtained Reynolds value is $Re_{70} \simeq 1.1 \times 10^5$. Hence, for each profile two polar curves are computed: one at $Re = 1 \times 10^5$ and one at $Re = 2 \times 10^5$. This provides for each profile a set of two polar curves. Then Dorothy LL-VP interpolates between those polar curves depending on the local Reynolds number computed using the local chord and true velocity (Equation (29)). The N_{crit}[54] is set to match the 2% upstream turbulence intensity. Confronting the obtained polar curves for NACA 63-418 and NACA 63-422 profiles to the literature[65] ensures they are of sufficient quality for computation. Figure C1 of Appendix C presents the NACA 63-418 polar curves at $Re = 2 \times 10^5$ over the full 360° range of angles of attack while Figure 11B focuses on $\alpha \in [-5°, +20°]$.

To lower the computational cost, the inter-particle spacing after redistribution (dh) is set to be slightly higher than d$r \simeq 1.2 \times 10^{-2}$ m. The redistribution is performed every 50 time-steps. Moreover, the turbines angular velocity (ω_{rot}) is set to match the experimental one at 8.0 rad·s^{-1}. Following Section 3.4, the associated time-step is chosen to obtain an angular step of 5°. The physical time of the computation (t_{max}) is chosen to have the start up vortices advected more than 10D away of the zone at interest that stops at 10D downstream of the two upstream turbines. Hence, approximately the last 700 iterations are available to compute velocity average for the wake velocity profiles (Figure 12) and the wake velocity map (Figure 13). Those computation parameters are summarized in Table 6. The number of CPUs (n_{CPU}) and the averaged computational time (t_{CPU}) needed to run the computations on AMD EPYC 9654 Genoa nodes are also specified in Table 6.
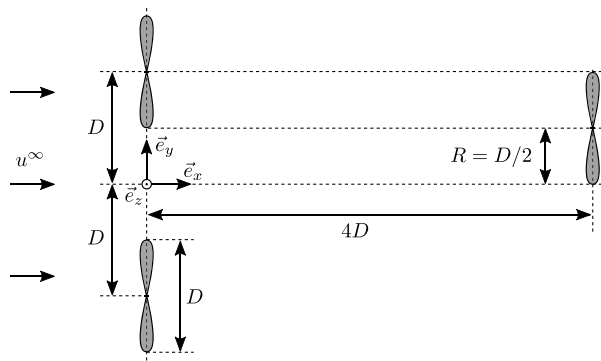
Two computations with the three turbines configuration are presented in this paper. A first one is carried out without upstream turbulence. It is used as a reference case and it is referred to as 'steady inflow'. A second one is carried out with the upstream turbulence following the

TABLE 4 IFREMER-LOMC turbine model properties.

R_h (m)	L_b (m)	N_s (-)	Pitch angle (°)
0.046	0.304	25	+4.87

TABLE 5 Upstream flow properties in front of the first row of turbines.

ρ (kg·m^{-3})	ν (m^2·s^{-1})	u^∞ (m·s^{-1})	σ_{u_x} (m·s^{-1})	$\sigma_{u_y} = \sigma_{u_z}$ (m·s^{-1})	L_I (m)	TI_{3D} (%)
10^3	10^{-6}	0.791	0.02	0.01	0.7	2.0

(A) Top view representation of the numerical set-up with the three tidal turbine models in interaction. The downstream turbine is partially immersed in the wake of an upstream one.
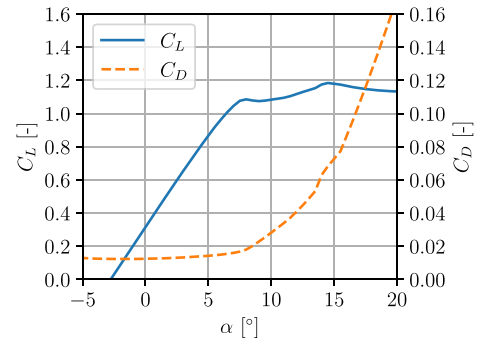
(B) NACA 63-418 polar curves computed at $Re = 2 \times 10^5$ for $\alpha \in [-5°, +20°]$.

FIGURE 11 An overview of the input data is provided with, on the left, the spatial representation of the three tidal turbines numerical experiment and, on the right, a zoom on one of the NACA 63-418 polar curves.

TABLE 6 Three turbines computations discretization and computational parameters.

dh (m)	TSR	ω_{rot} (rad·s^{-1})	dt (s)	dθ (°)	t_{max} (s)	n_{CPU} (-)	t_{CPU} (hh:mm:ss)
1.8×10^{-2}	$\simeq 3.5$	8.0	1.1×10^{-2}	5.0	17.0	384	18 : 56 : 24

specifications described above. It is the computation that represents as accurately as possible the IFREMER experimental conditions. It is referred to as 'TI 2' in the rest of the paper.

4.3.2 | Wake analysis

Figure 12 represents a velocity profiles comparison between the numerical results from Dorothy LL-VP (denoted 'Num.') and the experimental results from IFREMER. The profiles represent velocity averages on spatial lines normal to the upstream flow in the middle plane that contains the three centres of rotation. While the numerical results are represented with solid or dash-dotted lines, the experimental results are represented with black markers associated to the standard deviation. First, by studying the velocity profile upstream of the turbines at $x = -1D$, it is noticed that both 'steady inflow' and 'TI 2' cases show a good agreement with the experimental averaged velocity. The difference between 'steady inflow' and 'TI 2' can be explained by the limited duration on which the velocity is averaged. A longer averaging time would benefit to those results and enhance the convergence of the statistical properties of the turbulent inflow. Second, at both $x = 2D$ and $x = 3D$ positions, the velocity depletion in the upstream turbines wake is numerically underestimated. To the authors opinion, this must results from a combination of two effects. The Reynolds numbers at which are operated the turbine models in the experiment are within the transition range of the considered blade profiles. Hence, there is a significant uncertainty about the polar curves values and in the resulting numerical wake. Moreover, the flume tank blockage, partly due to free surface, is about 10 % in the considered experiment. This phenomenon is highlighted by the velocity increase in the by-pass areas around the two upstream turbines. In addition, the by-pass flow at each turbine rotation centre due to the absence of hub in the numerical turbine modelling seems to be nearly recovered at $x = 2D$ and is not noticeable at $x = 3D$. The flume tank blockage surely modifies the experimental turbine wakes compared to the numerical results where no blockage is modelled. Finally, the velocity profiles after the downstream turbine at $x = 5.2D$ and $x = 7D$, show a good agreement between numerical and experimental results. The wake mixing after the downstream turbine seems to be numerically well captured. It can be noticed that the upstream turbulence ('TI 2') seems to enhance far wake description with respect to the experiment compared to the numerical case without upstream turbulence ('steady inflow').

Figure 13 represents the normalized velocity map for the numerical results of the 'TI 2' case. Space dimensions are normalized by the turbine diameter D. Figure 13 is a full 2D representation of the spatially discretized velocity profiles previously presented in Figure 12. The black contour lines represent the demarcation between areas of same velocity as stated in the colour scale reported in Figure 13. The turbines are materialized by rectangles.

Figure 14 represents the vorticity map for the numerical results of the 'TI 2' case. In this figure, the black contour line represent the median vorticity value. Contrary to the velocity map, this vorticity map is an instantaneous field. Moreover, the presented vorticity is filtered from the
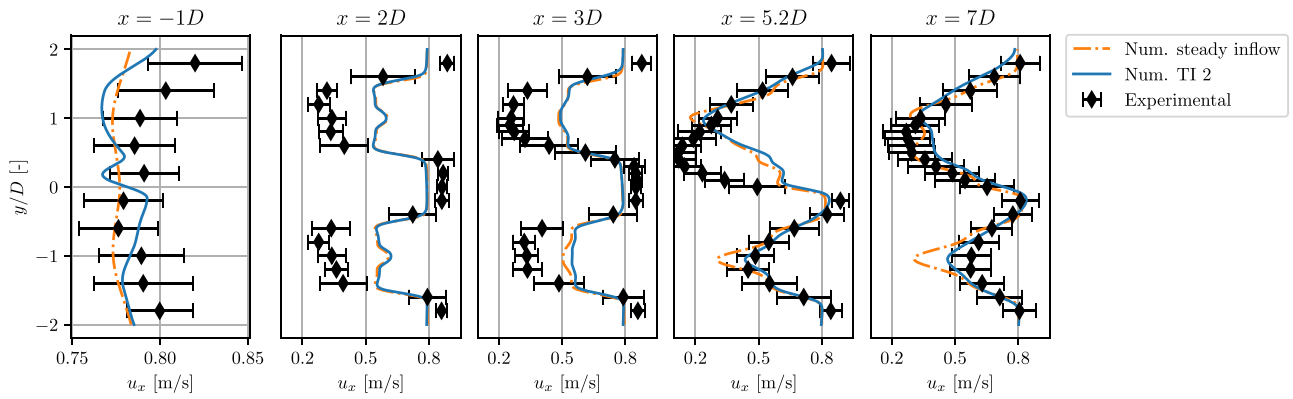
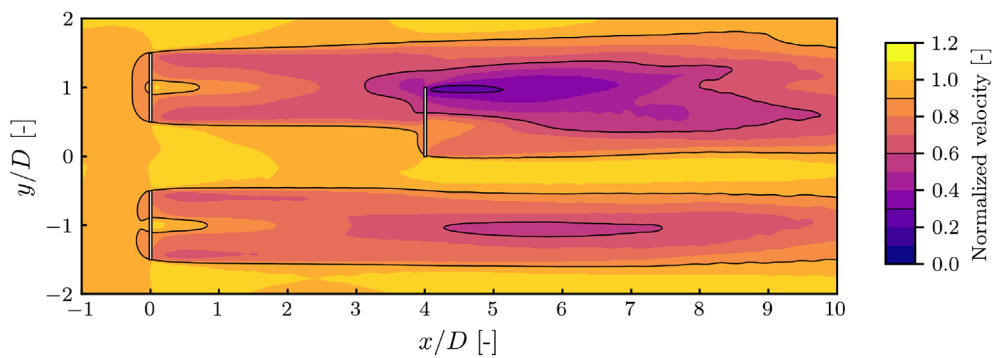**FIGURE 12** Comparison between numerical and experimental results on velocity profiles at different *x* positions.

FIGURE 13 2D map of the normalized velocity (u_x/u^∞) of the numerical 'TI 2' case.
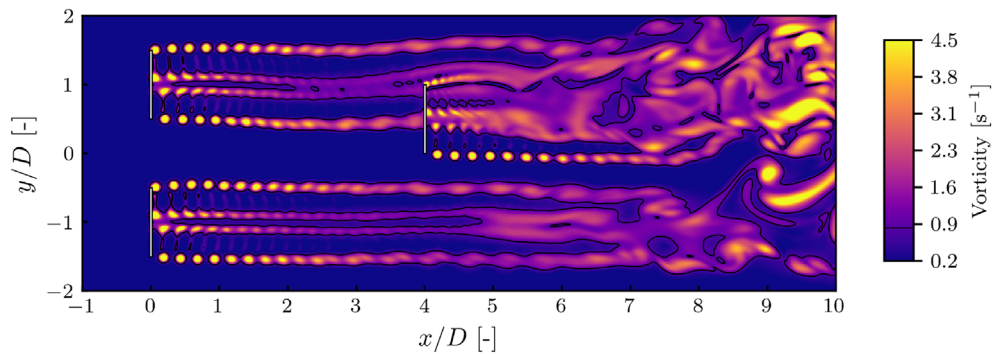
FIGURE 14 2D map of the vorticity of the numerical 'TI 2' case. Upstream turbulence induced vorticity is filtered.

upstream turbulence generated vorticity to enhance the map readability. Those elements result in a clean representation of the shed tip vortices. Around $2D$ downstream of each turbine, those vortices start to merge together and generate bigger structures. At $x/D \simeq 5$, the wake starts to be more turbulent at the centre and the tip vortices are completely merged. After $x/D \geq 7$, the wake is fully turbulent and no coherent structure can be noticed any longer. This visual description appears to be similar to the formal wake analysis presented in[66]. One of the upcoming works is to further confirm the correct behaviour of the presented LL-VP method on wake interaction. To achieve this, a thorough numerical reproduction of the IFREMER experiment will be studied with different positions for the downstream turbine at two different upstream turbulence intensities ($TI_{3D} \simeq 2\%$ or $TI_{3D} \simeq 16\%$).

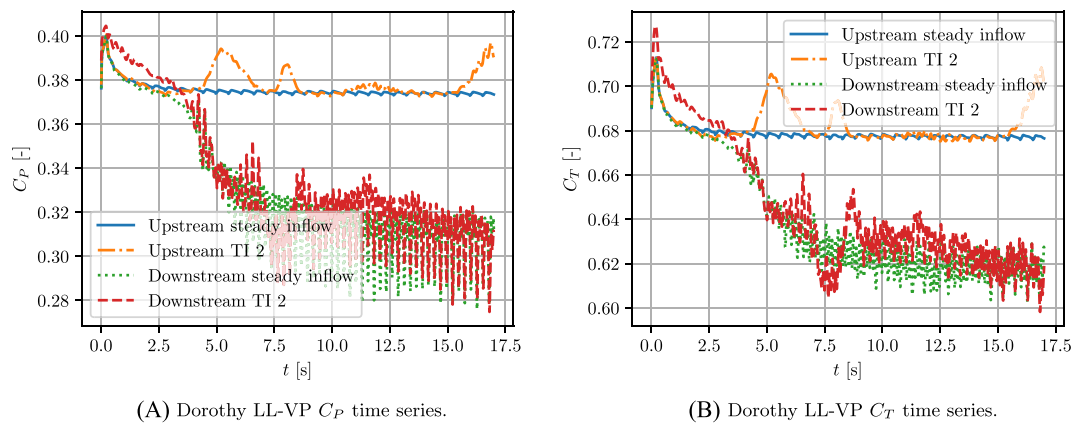(A) Dorothy LL-VP C_P time series. (B) Dorothy LL-VP C_T time series.

FIGURE 15 Time series of Dorothy LL-VP performance results from IFREMER-LOMC tidal turbine model at $TSR = 3.5$ and two different positions (upstream or downstream) immersed either in a steady inflow or an usptream turbulence of $TI_{3D} \simeq 2\%$.

4.3.3 | Performance and loads analysis

Figure 15 presents the time histories of the performance results: C_P on the left (Figure 15A) and C_T on the right (Figure 15B). The two computations, 'steady inflow' and 'TI 2', are represented. Moreover, results from either the upstream turbine located at $(-0.7,0,0)$ or the downstream one are reported, respectively denoted 'upstream' and 'downstream'. Those performance results are computed using Shen's tip correction for loads[48] as discussed in Section 4.2.2. When focusing on the upstream turbine in steady inflow results, it can be noticed that the redistribution generates a slight change in performance each time it is applied. Moreover, in all the results, a performance peak occurs during the first 3s of the time histories. To the authors opinion, this is due to the start up vortex of each turbine. The starting of the computation can be interpreted as an Heaviside function ranging from zero to the prescribed mean upstream flow velocity (u^∞). Hence a transient response of the turbine with this peak is generated. Such transient peaks have been described in the literature for instantaneous surge motions applied as an Heaviside function on offshore wind turbine[1] that are similar to the instantaneous velocity change of the present computations start. From 4s to 8s the regime of the downstream turbine performance changes significantly due to the wake of the upstream turbines that have an increasing impact on its behaviour. Finally, after 10s the computations reach a converged state from a wake conditions point of view. This is this dynamic regime that is studied in the rest of the paper. It can be observed that the upstream turbulence in the 'TI 2' case introduces low frequency and high amplitude variations of the performance of both the upstream or downstream turbine. The focus of the study is made on the downstream turbine with a turbulent upstream flow, 'TI 2' case, as it represents the closest numerical reproduction of the experiment.

First the turbine averaged performance and loads are studied. On the one hand, experimental results, from Gaurier et al.,[63] on the single turbine, similar to the upstream numerical turbine, show a $C_P = 0.43$ and a $C_T = 0.86$ at $TSR = 3.5$ with $TI_{3D} \simeq 2\%$. The experimental downstream turbine performance in the same conditions highlights a decrease of C_P to 0.28 (-35%) and C_T to 0.76 (-12%). On the other hand, the averaged performance of the upstream turbine of the numerical 'TI 2' case are $C_P = 0.38$ and a $C_T = 0.68$. The averaged performance of the downstream turbine numerically evaluated in the same conditions are $C_P = 0.31$ (-18%) and a $C_T = 0.62$ (-9%). To the authors opinion, the discrepancy between the experimental and numerical performance averages is due to the flume tank blockage in the experiment and the limited accuracy of the polar curves used in the numerical computations. Furthermore, the performance decrease of the downstream turbine can be interpreted using the radial distributions of angles of attack and loads depicted in Figure 16. Figure 16 shows the averaged radial distributions of angles of attack, normal force and tangential force respectively at the left (Figure 16A), centre (Figure 16B) and right (Figure 16C). As the downstream turbine suffers from a velocity depletion generated by the upstream turbine positioned at $(+0.7,0,0)$, this turbine experiences a lower averaged upstream velocity while rotating at the same imposed angular velocity as the upstream turbines. Thus, the angles of attack distribution is lower for the downstream turbine compared to the upstream one (Figure 16A). This explains the lower loads distributions of the downstream turbine compared to the upstream one (Figure 16B,C). It is reminded that the power and thrust coefficients (Equations (58) and (59)) are computed using the upstream velocity, which does not account of the velocity depletion experienced by the downstream turbine. Consequently, this study of blade radial angles of attack and loads confirms the performance decrease previously described.

Second, the downstream turbine performance fluctuations are studied through standard deviations and frequency analysis. On the one hand, experimental results on the downstream turbine, present a fluctuation level of $\sigma(C_P) = 0.05$ and $\sigma(C_T) = 0.07$ at $TSR = 3.5$ with $TI_{3D} \simeq 2\%$. Those standard deviation magnitudes represent respectively 12% and 8% of the average values. On the other hand, the numerical results on the downstream turbine of the 'TI 2' case recorded standard deviations of $\sigma(C_P) = 0.01$ and $\sigma(C_T) = 0.01$. Those standard deviation magnitudes represent respectively 3% and 1.5% of the averaged values, that is to say approximately four times lower than the fluctuations experimentally measured.
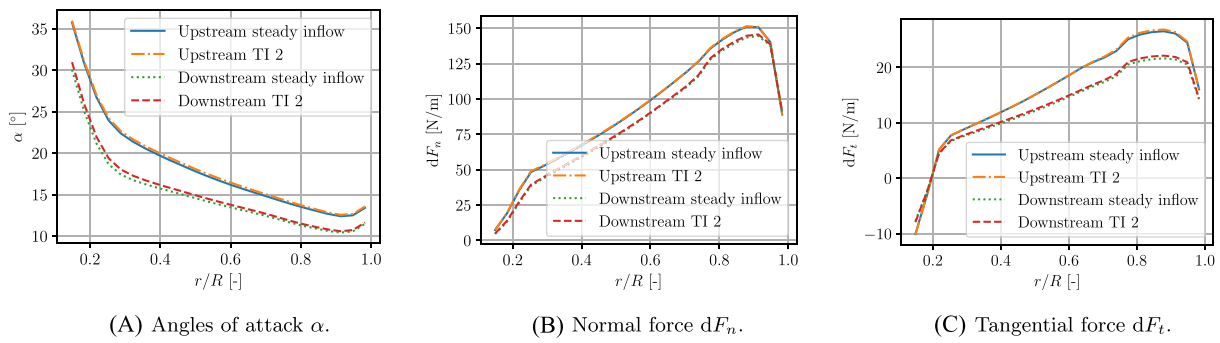
(A) Angles of attack α. (B) Normal force dF_n. (C) Tangential force dF_t.

FIGURE 16 Averaged radial distributions of angles of attack (α) and blade loads for the LOMC-IFREMER tidal turbine model at $TSR = 3.5$ and two different positions (upstream or downstream) immersed either in a steady inflow or an usptream turbulence of $TI_{3D} \simeq 2\%$
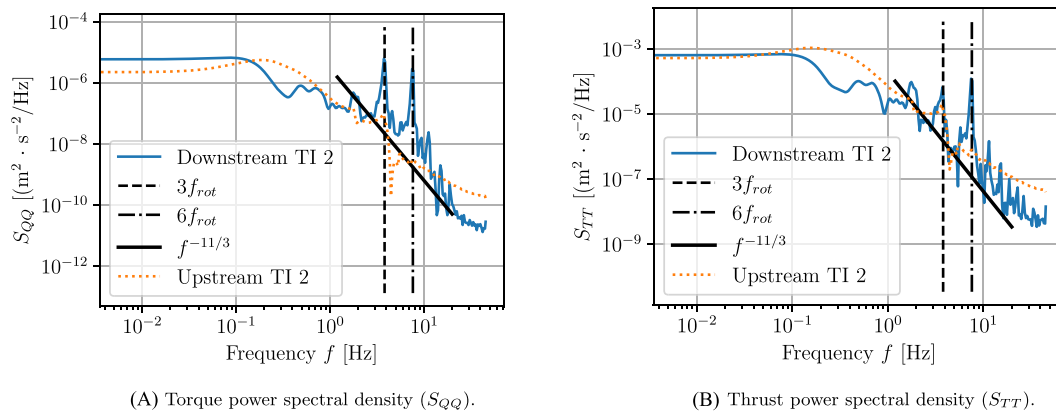

(A) Torque power spectral density (S_{QQ}). (B) Thrust power spectral density (S_{TT}).

FIGURE 17 Upstream and downstream turbines torque PSD (S_{QQ}) and thrust PSD (S_{TT}) for the numerical 'TI 2' case.

According to the authors, such low levels of fluctuations concerning the numerical results must result from too small time histories. Data samples of limited size prevent from having the upstream turbulence statistic properties converged. Thus, the resulting upstream turbulence induced fluctuations must also not be converged. The aim in a near future is to perform such numerical computations for significantly longer physical time. Moreover, the limited accuracy of the polar curves must have played a role in this low fluctuations evaluation. The numerical performance time series of the downstream turbine (Figure 15) show a combination of low frequency variations due to the upstream turbulence and high frequency fluctuations. Those high frequency fluctuations are also noticeable for the downstream turbine in the steady inflow case. This is the reason why they are interpreted to be a consequence of the upstream wake presence. Hence, those high frequency fluctuations can be studied from a frequency point of view. Figure 17 represents the spectral results through power spectral densities (PSD)[67] of the torque (S_{QQ}, Figure 17A) and thrust PSD (S_{TT}, Figure 17B). Only the numerical results with a turbulent upstream flow, 'TI 2' case, are represented in Figure 17A,B. The reader can easily notice that both torque and thrust PSD spectra of the downstream turbine show high levels for three times the rotation frequency, denoted $3f_{rot}$, and six times this rotation frequency, denoted $6f_{rot}$. Consequently, the high frequency fluctuations previously observed in the downstream turbine time histories must result from those specific frequencies: $3f_{rot}$ and $6f_{rot}$. Those frequency components can be interpreted as the downstream turbine blades interaction with the velocity shear between the two zones of the flow encountered by this turbine: one around the mean upstream velocity (u^∞) and one in the wake of the upstream turbine. Finally, both torque and thrust PSD spectra of the upstream and downstream turbines seem to follow a $f^{-11/3}$ power law as represented in Figure 17A,B. This phenomenon is linked to torque and thrust dependency to upstream turbulence as experimentally shown in Druault et al.[68] Finally, the general aspect of those numerical spectra is very similar to the one presented for the experimental results in Gaurier et al.[63]

5 | CONCLUSION

To summarize, this paper presented a new lifting-line implementation within the Lagrangian vortex particle method (LL-VP). The advantages of such an LL-VP method compared to vortex filament codes is the ability to account for diffusion in the Navier-Stokes equations, possibly with an

LES model. It can also account for complex onset flows: namely, upstream ambient turbulence and upstream turbine wake as shown in the case of three interacting turbines (Section 4.3.3).

After having recalled the vortex particle method framework, the present paper details a new vortex particles shedding strategy following the lifting-line approach. Some key definitions as the shed particles definition are provided for coders to be able to reproduce the present method. The presented LL-VP method shows accurate results on cases of increasing complexity through the paper. First, the elliptic wing case highlights the convergence of the numerical results towards the analytical solution available for this specific wing. Second, the study of the New MEXICO rotor shows that the presented LL-VP method is capable to give accurate angles of attack and loads results for three different tip speed ratios. Velocity profiles in the wake close to the rotor are studied with accurate results obtained from the present LL-VP with respect to experimental or other numerical results. Finally, the present LL-VP is used to analyse complex onset flow structures on a case representing three tidal turbines models with one of them being downstream of the wake generated by the two upstream ones. Those preliminary results are promising at different levels. A favourable agreement with experimental data is obtained on wake maps and specific velocity profiles at different positions downstream of the turbines. Wake length as well as velocity deficit and general shape are all important features when coming to wind and tidal turbines farm design. Moreover, LL-VP performance results of the downstream turbine reproduce means and standards deviations with a reasonable accuracy when compared to experimental results. The loads spectra match the expected decrease rate in the high frequency domain which is an element in favour of the accurate reproduction of this complex flow by the LL-VP method.

For all these reasons, the presented LL-VP method can be considered as validated. Its implementation in the Dorothy solver will be a useful tool for upcoming works which raise some interesting and promising perspectives in a near future. One of them could be longer computations on similar turbines farm configurations to offer the possibility to compute damage equivalent load (DEL) for the downstream turbines. This would be helpful to decrease uncertainty on material fatigue for floating offshore wind turbines or tidal turbines. It can also be imagined to use this LL-VP tool to optimize a minimal space-filling geometry on a limited number of turbines so as to optimize a farm with given site-dependant meteocean conditions. Although some code optimizations are still required, this could allow to optimize a farm at an affordable computational cost. It is even possible to address the issue of a turbine working at a degraded operating point in case of the failure of some controlling device. For instance, the consequences of a turbine working at modified, yaw, pitch, tip speed ratio or with a single-blade pitch failure on itself and on a farm could be tackled.

PEER REVIEW

The peer review history for this article is available at https://www.webofscience.com/api/gateway/wos/peer-review/10.1002/we.2905.

Data Availability Statement

Data not available due to legal restrictions.

ORCID

M.-A. Dufour https://orcid.org/0000-0003-0808-1856

G. Pinon https://orcid.org/0000-0002-9708-1219

F. Blondel https://orcid.org/0000-0002-3252-2781

G. Germain https://orcid.org/0000-0002-8324-5104

REFERENCES

1. Corniglion R, Harris JC, Peyrard C. The aerodynamics of a blade pitch, rotor speed, and surge step for a wind turbine regarding dynamic inflow. *Wind Energy*. 2022;25(5):858-880.
2. van Garrel A. Development of a Wind Turbine Aerodynamics Simulation Module. Energy research Centre of the Netherlands; 2003.
3. Murray J, Barone M. The Development of CACTUS, a Wind and Marine Turbine Performance Simulation Code. In: 49th AIAA Aerospace Sciences Meeting including the New Horizons Forum and Aerospace Exposition. American Institute of Aeronautics and Astronautics; 2011; Orlando, Florida.
4. Sebastian T, Lackner MA. Development of a free vortex wake method code for offshore floating wind turbines. *Renew Energy*. 2012;46(0):269-275.

5. Berdowski T. Three-dimensional free-wake vortex simulations of an actuator disc in yaw and tilt. In: 2018 Wind Energy Symposium. American Institute of Aeronautics and Astronautics; 2018; Kissimmee, Florida.

6. Shaler K, Branlard E, Platt A. OLAF User's Guide and Theory Manual. NREL/TP-5000-75959, 1659853, MainId:6799, National Renewable Energy Laboratory; 2020.

7. Prandtl L. Applications of modern hydrodynamics to aeronautics. NACA-TR-116, National Advisory Committee for Aeronautics; 1923.

8. Phillips WF, Snyder DO. Modern Adaptation of Prandtl's Classic Lifting-Line Theory. *J Aircraft*. 2000;37(4):662-670.

9. Katz J, Plotkin A. *Low-Speed Aerodynamics*. 2nd Edition: Cambridge University Press; 2001.

10. Bénard P, Viré A, Moureau V, Lartigue G, Beaudet L, Deglaire P, Bricteux L. Large-eddy simulation of wind turbines wakes including geometrical effects. *Comput Fluids*. 2018;173:133-139.

11. Mullings H, Stallard T. Analysis of tidal turbine blade loading due to blade scale flow. *J Fluids Struct*. 2022;114:103698.

12. Ouro P, Mullings H, Stallard T. Establishing confidence in predictions of fatigue loading for floating tidal turbines based on large-eddy simulations and unsteady blade element momentum. *Trends in Renewable Energies Offshore*. 1st ed. London: CRC Press; 2022:915-924.

13. Rosenhead L. The formation of vortices from a surface of discontinuity. *Proc Royal Soc London*. 1931;A(134):170-192.

14. Rehbach C. Numerical calculation of three-dimensional unsteady flows with vortex sheets. In: 16th Aerospace Sciences Meeting. American Institute of Aeronautics and Astronautics; 1978; Huntsville,AL,U.S.A.

15. Leonard A. Vortex methods for flow simulation. *J Comput Phys*. 1980;37(3):289-335.

16. Lewis RI. *Vortex Element Methods for Fluid Dynamic Analysis of Engineering Systems*: Cambridge University Press; 1991.

17. Winckelmans GS, Leonard A. Contributions to vortex particle methods for the computation of three-dimensional incompressible unsteady flows. *J Comput Phys*. 1993;109(2):247-273.

18. Cottet G-H, Koumoutsakos PD. *Vortex Method : Theory and Practice*: Cambridge University Press, UK; 2000.

19. Zervos A, Huberson S, Hemon A. Three-dimensional free wake calculation of wind turbine wakes. *J Wind Eng Ind Aerodyn*. 1988;27(1–3):65-76.

20. Voutsinas SG, Riziotis VA. Dynamic stall and 3D effects, National Technical University of Athens - JOU2-CT93-0345; 1996.

21. Hansen MOL, Sørensen JN, Voutsinas S, Sørensen N, Madsen HA. State of the art in wind turbine aerodynamics and aeroelasticity. *Progr Aerosp Sci*. 2006;42(4):285-330.

22. Baltazar J, Falcão de Campos JAC. Hydrodynamic analysis of a horizontal axis marine current turbine with a boundary element method. In: Proceedings of the ASME 27th conference on offshore mechanics and arctic engineering (OMAE). ASME; 2008:883-893.

23. Pinon G, Mycek P, Germain G, Rivoalen E. Numerical simulation of the wake of marine current turbines with a particle method. *Renew Energy*. 2012; 46(0):111-126.

24. Chatelain P, Backaert S, Winckelmans G, Kern S. Large eddy simulation of wind turbine wakes. *Flow, Turbulence Combust*. 2013;91(3):587-605.

25. Chatelain P, Duponcheel M, Zeoli S, Buffin S, Caprace D-G, Winckelmans G, Bricteux L. Investigation of the effect of inflow turbulence on vertical axis wind turbine wakes. *J Phys: Confer Ser (Print)*. 2017;854(1):12011.

26. Mycek P, Pinon G, Lothodé C, Dezotti A, Carlier C. Iterative solver approach for turbine interactions: application to wind or marine current turbine farms. *Appl Math Model*. 2017;41:331-349.

27. Mycek P. étude numérique et expérimentale du comportement d'hydroliennes. *Ph.D. Thesis*: Université du Havre; 2013.

28. Pinon G, Carlier C, Fur A, Gaurier B, Germain G, Rivoalen E. Account of ambient turbulence for turbine wakes using a Synthetic-Eddy-Method. *J Phys: Confer Ser*. 2017;854(1):12016.

29. Choma Bex C, Carlier C, Fur A, Pinon G, Germain G, Rivoalen E. A stochastic method to account for the ambient turbulence in Lagrangian Vortex computations. *Appl Math Model*. 2020;88:38-54.

30. Alvarez EJ, Ning A. High-fidelity modeling of multirotor aerodynamic interactions for aircraft design. *AIAA J*. 2020;58(10):4385-4400.

31. Tugnoli M, Montagnani D, Syal M, Droandi G, Zanotti A. Mid-fidelity approach to aerodynamic simulations of unconventional VTOL aircraft configurations. *Aerosp Sci Technol*. 2021;115:106804.

32. Ramos-García N, Hejlesen MM, Sørensen JN, Walther JH. Hybrid vortex simulations of wind turbines using a three-dimensional viscous–inviscid panel method. *Wind Energy*. 2017;20(11):1871-1889.

33. Beale JT, Majda A. High order accurate vortex methods with explicit velocity kernels. *J Comput Phys*. 1985;58(2):188-208.

34. von Helmholtz H. über Integrale der hydrodynamischen Gleichungen, welche den Wirbelbewegungen entsprechen. *Journal für die reine und angewandte Mathematik (Crelles Journal)*. 1858;55:25-55.

35. Poisson S-D. Remarques sur une équation qui se présente dans la théorie des attractions des sphéroïdes. *Nouveau Bulletin des Sciences : Par La Société Philomat(h)ique (de Paris)*. 1813;3(75):388-392.

36. Jarrin N, Benhamadouche S, Laurence D, Prosser R. A synthetic-eddy-method for generating inflow conditions for large-eddy simulations. *Int J Heat Fluid Flow*. 2006;27:585-593.

37. Lindsay K, Krasny R. A particle method and adaptive treecode for vortex sheet motion in three-dimensional flow. *J Comput Phys*. 2001;172(2):879-907.

38. Greengard L, Rokhlin V. A fast algorithm for particle simulations. *J Comput Phys*. 1987;73(2):325-348.

39. Mansfield JR, Knio OM, Meneveau C. A dynamic LES scheme for the vorticity transport equation: formulation and a priori tests. *J Comput Phys*. 1998; 145(2):693-730.

40. Choquin J-P, Cottet G-H. Sur l'analyse d'une classe de méthodes de vortex tridimensionnelles. *Comptes Rendus Hebdomadaires des Séances de l'Académie des Sciences*. 1988;306(17):739-742.

41. Winckelmans GS. Topics in vortex methods for the computation of three- and two-dimensional incompressible unsteady flows. *Ph.D. Thesis*: California Institute of Technology; 1989.

42. Degond P, Mas-Gallic S. The weighted particle method for convection-diffusion equations—part II : the anisotropic case. *Math Comput*. 1989;53:509-526.

43. Choquin JP, Huberson S. Particles simulation of viscous flow. *Comput Fluids*. 1989;17(2):397-410.

44. Rivoalen E, Huberson S. The particle strength exchange method applied to axisymmetric viscous flows. *J Comput Phys*. 2001;168(2):519-526.

45. Mycek P, Pinon G, Germain G, Rivoalen E. A self-regularising DVM–PSE method for the modelling of diffusion in particle methods. *Comptes Rendus Mécanique*. 2013;341(9–10):709-714.

46. Mansour NN, Ferziger JH, Reynolds WC. Large-eddy simulation of a turbulent mixing layer, Report TF-11, Thermosciences Div., Dept. of Mech. Eng., Stanford University; 1978.
47. Smagorinsky J. General circulation experiments with the primitive equations. I. The basic experiment. *Monthly Weather Rev*. 1963;91:99-164.
48. Shen WZ, Mikkelsen R, Sørensen JN, Bak C. Tip loss corrections for wind turbine computations. *Wind Energy*. 2005;8(4):457-475.
49. Wimshurst A, Willden RHJ. Analysis of a tip correction factor for horizontal axis turbines: analysis of a tip correction factor for horizontal axis turbines. *Wind Energy*. 2017;20(9):1515-1528.
50. Ploumhans P, Winckelmans GS. Vortex methods for high resolution simulations of viscous flow past bluff-bodies of general geometry. *J Comput Phys*. 2000;165:354-406.
51. Carmichael R. Algorithm for calculating coordinates of cambered NACA airfoils at specified chord locations. In: 1st AIAA, Aircraft, Technology Integration, and Operations Forum. American Institute of Aeronautics and Astronautics; 2001; Los Angeles,CA,U.S.A.
52. Drela M, Giles MB. Viscous-inviscid analysis of transonic and low Reynolds number airfoils. *AIAA J*. 1987;25(10):1347-1355.
53. Drela M. XFOIL: an analysis and design system for low Reynolds number airfoils. In: Mueller TJ, ed. *Low Reynolds number aerodynamics*, Vol. 54. Berlin, Heidelberg: Springer Berlin Heidelberg; 1989:1-12.
54. van Ingen J. The eN method for transition prediction. Historical review of work at TU Delft. In: 38th Fluid Dynamics Conference and Exhibit. American Institute of Aeronautics and Astronautics; 2008; Seattle, Washington.
55. Viterna LA, Janetzke DC. Theoretical and experimental power from large horizontal-axis wind turbines. DOE/NASA/20320-41; NASA-TM-82944, Cleveland, OH (United States), NASA Lewis Research Center; 1982.
56. Hoerner SF. *Fluid-Dynamic Drag: Theoretical, Experimental and Statistical Information*: Hoerner Fluid Dynamics; 1965.
57. Schepers JG, Lutz T, Boorsma K, Gomez-Iradi S, Herraez I, Oggiano L, Rahimi H, Schaffarczyk P, Pirrung G, Madsen HA, Shen WZ, Weihing P. Final Report of IEA Wind Task 29 Mexnext (Phase 3). *Technical*. ECN-E–18-003, Energieonderzoek Centrum Nederland; 2018.
58. Corniglion R. Aero-elastic modeling of floating wind turbines with vortex methods. *These de Doctorat*: Marne-lavallée, ENPC; 2022.
59. Wimshurst A, Willden RHJ. Extracting lift and drag polars from blade-resolved computational fluid dynamics for use in actuator line modelling of horizontal axis turbines: Extracting lift and drag polars from blade-resolved computational fluid dynamics. *Wind Energy*. 2017;20(5):815-833.
60. Zilic de Arcos F, Vogel CR, Willden RHJ. Extracting angles of attack from blade-resolved rotor CFD simulations. *Wind Energy*. 2020;23(9):1868-1885.
61. Blondel F, Ferrer G, Cathelain M, Teixeira D. Improving a BEM yaw model based on New Mexico experimental data and vortex/CFD simulations. In: Congrès Français de Mécanique; 2017; Lille, France.
62. Gaurier B, Germain G, Facq J-V, Bacchetti T, Carlier C, Pinon G. Three tidal turbines in interaction: An experimental data-set on wake and performances *Edited by* SEANOE. ; 2018.
63. Gaurier B, Carlier C, Germain G, Pinon G, Rivoalen E. Three tidal turbines in interaction: an experimental study of turbulence intensity effects on wakes and turbine performance. *Renew Energy*. 2020;148:1150-1164.
64. Mycek P, Gaurier B, Germain G, Pinon G, Rivoalen E. Experimental study of the turbulence intensity effects on marine current turbines behaviour. Part I: one single turbine. *Renew Energy*. 2014;66(0):729-746.
65. Bertagnolio F, Sørensen N, Johansen J, Fuglsang P. *Wind Turbine Airfoil Catalogue*, Risoe-R. Denmark: Forskningscenter Risoe; 2001.
66. Houtin-Mongrolle F, Benard P, Lartigue G, Moureau V. A level-set framework for the wind turbine wake analysis: from high-fidelity unsteady simulations to 1D momentum theory. *J Phys: Confer Ser*. 2021;1934(1):12011.
67. Welch P. The use of fast Fourier transform for the estimation of power spectra: a method based on time averaging over short, modified periodograms. *IEEE Trans Audio Electroacoust*. 1967;15(2):70-73.
68. Druault P, Gaurier B, Germain G. Spatial integration effect on velocity spectrum: towards an interpretation of the - 11/3 power law observed in the spectra of turbine outputs. *Renew Energy*. 2022;181:1062-1080.
69. Barton G. *Elements of Green's Functions and Propagation: Potentials, Diffusion, and Waves*, Oxford Science Publications. Oxford : New York: Clarendon Press ; Oxford University Press; 1989.

APPENDIX A: Supplements to the vortex particle method background

A.1 | Poisson's equation solution

The aim of Appendix A.1 is to explain Poisson's equation solution. This solution is the origin of the Biot-Savart law (Equation (10)). First, the 3D Poisson's equation (Equation (A1)) is studied. δ stands for the Dirac's function.

$$-\Delta G\left(\vec{x}\right) = \delta\left(\vec{x}\right) \tag{A1}$$

As shown in Barton,[69] the solution to this equation is the 3D Green's function G that tends to zero at infinity, defined in Equation (8). Yet, the solution to Equation (7) being looked for is the function $\vec{\Psi}$. The Fourier transform of Equation (A1) becomes

$$\widehat{G}\left(\vec{\xi}\right) = \sigma\left(\vec{\xi}\right), \tag{A2}$$

where $\vec{\xi}$ is the spatial wavenumber and $\sigma\left(\vec{\xi}\right) = \frac{1}{\|\vec{\xi}\|^2} = \frac{1}{\xi_x^2 + \xi_y^2 + \xi_z^2}$ is the symbol of Laplacian operator in the Fourier domain. On the one hand, Equation (A2) is multiplied by the Fourier transform of the vorticity in the spatial domain $\left(\widehat{\vec{\omega}}\left(\vec{\xi}, t\right)\right)$:

$$\widehat{G}\left(\vec{\xi}\right)\widehat{\vec{\omega}}\left(\vec{\xi}, t\right) = \sigma\left(\vec{\xi}\right)\widehat{\vec{\omega}}\left(\vec{\xi}, t\right). \tag{A3}$$

On the other hand, the Fourier transform of Equation (7) is evaluated. Note that the symbol of Laplacian operator in the Fourier domain is known.

$$\widehat{\vec{\Psi}}\left(\vec{\xi}, t\right) = \sigma\left(\vec{\xi}\right)\widehat{\vec{\omega}}\left(\vec{\xi}, t\right) \tag{A4}$$

Terms' identification between Equations (A3) and (A4) provides Equation (A5).

$$\widehat{\vec{\Psi}}\left(\vec{\xi}, t\right) = \widehat{G}\left(\vec{\xi}\right)\widehat{\vec{\omega}}\left(\vec{\xi}, t\right) \tag{A5}$$

Equation (A5) is now written into the spatial domain. $\star$ denotes the convolution product.

$$\vec{\Psi}\left(\vec{x}, t\right) = G\left(\vec{x}\right) \star \vec{\omega}\left(\vec{x}, t\right) = \iiint_{\vec{y} \in \mathbb{R}^3} G\left(\vec{x} - \vec{y}\right)\vec{\omega}\left(\vec{y}, t\right) dv\left(\vec{y}\right) \tag{A6}$$

A.2 | Vortex particle method regularized kernel definition

The aim of Appendix A.2 is to briefly explain the principle behind the regularized vortex particle method. This methodology is thoroughly studied in the literature.[17,18,27,33] To circumvent the singular behaviour, a smoothing function (ζ_ε) is introduced to regularize the vorticity field. ζ_ε is defined from a radially symmetric function (ζ) such that

$$\zeta_\varepsilon\left(\vec{x}\right) = \frac{1}{\varepsilon^3}\zeta\left(\frac{\vec{x}}{\varepsilon}\right). \tag{A7}$$

In this definition, ε represents the cut-off or smoothing parameter, a well known parameter in the Lagrangian vortex community. It physically represents the radial distance on which the smoothing function has an influence. Making use of this smoothing function, the regularized vorticity field $\vec{\omega}_\varepsilon$ is defined from the vorticity field as

$$\vec{\omega}_\varepsilon\left(\vec{x}, t\right) = \zeta_\varepsilon\left(\vec{x}\right) \star \vec{\omega}\left(\vec{x}, t\right). \tag{A8}$$

Recalling the definition of vorticity (Equation (3)), the regularized vorticity can also be obtained by evaluating the curl of a regularized velocity field ($\vec{u}_\varepsilon^\Psi$), which is different from the velocity field ($\vec{u}^\Psi$). And $\vec{u}_\varepsilon^\Psi$ comes from the curl of a regularized potential vector ($\vec{\Psi}_\varepsilon$), different from $\vec{\Psi}$. The following equation is obtained:

$$\vec{\omega}_\varepsilon = \vec{\nabla} \times \vec{u}_\varepsilon = \vec{\nabla} \times \left(\vec{\nabla} \times \vec{\Psi}_\varepsilon\right). \tag{A9}$$

Following a similar process as obtaining Equation (7):

$$-\Delta \vec{\Psi}_\varepsilon = \vec{\omega}_\varepsilon. \tag{A10}$$

From the result of Equations (9) and (A8), and recalling the commutative nature of convolution product, the following equation is obtained:

$$\vec{\Psi}_\varepsilon\left(\vec{x},t\right) = G\left(\vec{x}\right) \star \vec{\omega}_\varepsilon\left(\vec{x},t\right) = G\left(\vec{x}\right) \star \zeta_\varepsilon\left(\vec{x}\right) \star \vec{\omega}\left(\vec{x},t\right) = G_\varepsilon\left(\vec{x}\right) \star \vec{\omega}\left(\vec{x},t\right), \tag{A11}$$

with G_ε being the regularized version of G, the Green's function introduced in Equation (8). It is not straightforward to evaluate the term $G_\varepsilon = G \star \zeta_\varepsilon$. The approach to solve this issue is to evaluate directly $\vec{\Psi}_\varepsilon$. This means finding directly a solution to Poisson Equation (A10). This process lasts from Equations (A12) to (A20). Then $\vec{u}_\varepsilon^\Psi$ is evaluated by taking the curl of the obtained definition for $\vec{\Psi}_\varepsilon$. Evaluating the curl of $\vec{\Psi}_\varepsilon$ eventually provides with a definition for the regularized kernels. This process lasts from Equation (A21) to Equation (A24). First, an hypothetical radially symmetric function $F : \mathbb{R} \to \mathbb{R}$ is defined as the solution to Equation (A12).

$$\Delta F = -\zeta \tag{A12}$$

The regularized function F_ε is defined by

$$\begin{aligned} F_\varepsilon : \quad \mathbb{R}^3 \quad &\to \quad\quad\quad \mathbb{R} \\ \vec{x} \quad &\mapsto \quad F_\varepsilon(\vec{x}) = \frac{1}{\varepsilon} F\left(\frac{\|\vec{x}\|}{\varepsilon}\right). \end{aligned} \tag{A13}$$

The function H is defined to ease vector calculus with F_ε:

$$\begin{aligned} H : \quad \mathbb{R} \quad &\to \quad\quad \mathbb{R} \\ r \quad &\mapsto \quad H(r) = \frac{1}{\varepsilon} r. \end{aligned} \tag{A14}$$

Then, $F_\varepsilon(\vec{x}) = \frac{1}{\varepsilon}(F \circ H)(\|\vec{x}\|)$. Note that $dH/dr = 1/\varepsilon$. It is reminded that the objective is to obtain directly a solution to Equation (A10). To this end, the following Laplacian, expressed in spherical coordinates with the radius magnitude as variable, is evaluated:

$$\begin{aligned} \Delta(F \circ H)(r) \;\; &= \frac{d^2}{dr^2}(F \circ H)(r) + \frac{2}{r}\frac{d}{dr}(F \circ H)(r) \\ &= \frac{d}{dr}\left(\frac{dH}{dr}(r)\left(\frac{dF}{dr} \circ H\right)(r)\right) + \frac{2}{r}\frac{dH}{dr}(r)\left(\frac{dF}{dr} \circ H\right)(r) \\ &= \left[\frac{d^2 H}{dr^2}(r)\left(\frac{dF}{dr} \circ H\right)(r) + \left(\frac{dH}{dr}(r)\right)^2\left(\frac{d^2 F}{dr^2} \circ H\right)(r)\right] \\ &\quad + \frac{2}{H(r)}\frac{1}{\varepsilon}\frac{dH}{dr}(r)\left(\frac{dF}{dr} \circ H\right)(r) \\ &= \frac{1}{\varepsilon^2}\left(\left(\frac{d^2 F}{dr^2} \circ H\right)(r) + \frac{2}{H(r)}\left(\frac{dF}{dr} \circ H\right)(r)\right) \\ &= \frac{1}{\varepsilon^2}[\Delta F(\rho)]_{\rho = H(r)}. \end{aligned}$$

Now that the Laplacian of the composed function $F \circ H$ is known, the Laplacian of F_ε can be evaluated. It is reminded that F is defined such that Equation (A12) is verified. It is reminded here that, in Equation (A15), the smoothing function definition from Equation (A7) is used.

$$\Delta F_\varepsilon(\vec{x}) = \frac{1}{\varepsilon}\Delta(F \circ H)(\|\vec{x}\|) = \frac{1}{\varepsilon^3}[\Delta F(\rho)]_{\rho = H(\|\vec{x}\|)} \tag{A15}$$

$$= \frac{1}{\varepsilon^3} [-\zeta(\rho)]_{\rho = H(\|\vec{x}\|)} = -\zeta_\varepsilon(\vec{x}) \tag{A16}$$

Let us now prove that $F_\varepsilon \star \vec{\omega}$ is a solution of Poisson equation (Equation (A10)). It is again assumed that all the hypothesis to invert partial derivatives and integrals are met.

$$\Delta_x \left(F_\varepsilon \star \vec{\omega} \right) = \Delta_x \left(\iiint_{\vec{y} \in \mathbb{R}^3} F_\varepsilon \left(\vec{x} - \vec{y} \right) \vec{\omega} \left(\vec{y}, t \right) dv \left(\vec{y} \right) \right) \tag{A17}$$

$$= \iiint_{\vec{y} \in \mathbb{R}^3} \vec{\omega} \left(\vec{y}, t \right) \Delta_x F_\varepsilon \left(\vec{x} - \vec{y} \right) dv \left(\vec{y} \right) \tag{A18}$$

$$= \Delta_x F_\varepsilon \star \vec{\omega} = -\zeta_\varepsilon \star \vec{\omega} = -\vec{\omega}_\varepsilon \tag{A19}$$

This eventually proves that

$$\vec{\Psi}_\varepsilon = F_\varepsilon \star \vec{\omega}. \tag{A20}$$

Now that the regularized vector potential is known, the velocity is evaluated by taking the curl of the vector potential $\vec{\Psi}_\varepsilon$, as it is done in Equation (10). One easily recognizes the regularized Biot-Savart relation in Equation (A21).

$$\vec{u}_\varepsilon^\Psi \left(\vec{x}, t \right) = \iiint_{\vec{y} \in \mathbb{R}^3} \left(\vec{\nabla} F_\varepsilon \left(\vec{x} - \vec{y} \right) \right) \times \vec{\omega} \left(\vec{y}, t \right) dv \left(\vec{y} \right) = \iiint_{\vec{y} \in \mathbb{R}^3} \vec{K}_\varepsilon \left(\vec{x} - \vec{y} \right) \times \vec{\omega} \left(\vec{y}, t \right) dv \left(\vec{y} \right) \tag{A21}$$

Eventually, the last term to be evaluated is the gradient of F_ε function. The regularized velocity kernel is defined by $\vec{K}_\varepsilon(\vec{x}) = \vec{\nabla} F_\varepsilon(\vec{x})$. To reach the aim of evaluating this gradient, a new function has to be introduced: q. Let q be the primitive of function $r \mapsto r^2 \zeta(r)$. This definition immediately gives

$$q(\rho) = \int_0^\rho r^2 \zeta(r) dr. \tag{A22}$$

Recalling Equation (A12) and using again the Laplacian definition in spherical coordinates, Equation (A23) is obtained.

$$\frac{q(\rho)}{\rho^3} = \frac{1}{\rho^3} \int_0^\rho r^2 \frac{1}{r^2} \frac{d}{dr} \left(r^2 \frac{dF}{dr}(r) \right) dr = \frac{1}{\rho^3} \rho^2 \frac{dF}{d\rho} = \frac{1}{\rho} \frac{dF}{d\rho} \tag{A23}$$

The following notation is used: $q \circ H(\rho) = q_\varepsilon(\rho)$. All the tools are now available to evaluate the specific gradient: $\vec{\nabla} F_\varepsilon(\vec{x})$. This eventually provides the definition of the regularized kernel ($\vec{K}_\varepsilon(\vec{x})$).

$$\vec{K}_\varepsilon(\vec{x}) = \vec{\nabla} F_\varepsilon(\vec{x}) = \frac{1}{\varepsilon} \vec{\nabla} (F \circ H)(\|\vec{x}\|) = \frac{1}{\varepsilon} \left[\frac{d}{dr}(F \circ H)(r) \right]_{r = \|\vec{x}\|} \frac{\vec{x}}{\|\vec{x}\|} \tag{A24}$$

$$= \frac{1}{\varepsilon} \left[\frac{dH}{dr}(r) \left(\frac{dF}{dr} \circ H \right)(r) \right]_{r = \|\vec{x}\|} \frac{\vec{x}}{\|\vec{x}\|} \tag{A25}$$

$$= \frac{\vec{x}}{\varepsilon^2} \left[\frac{1}{r} \left(\frac{dF}{dr} \circ H \right)(r) \right]_{r = \|\vec{x}\|} \tag{A26}$$

$$= \frac{\vec{x}}{\varepsilon^3} \left[\frac{1}{H(r)} \left(\frac{\mathrm{d}F}{\mathrm{d}r} \circ H \right)(r) \right]_{r=\|\vec{x}\|} \tag{A27}$$

$$= \frac{\vec{x}}{\varepsilon^3} \left[\frac{1}{\rho} \frac{\mathrm{d}F}{\mathrm{d}\rho}(\rho) \right]_{\rho = H(\|\vec{x}\|)} = -\frac{\vec{x}}{\varepsilon^3} \left[\frac{q(\rho)}{\rho^3} \right]_{\rho = H(\|\vec{x}\|)} \tag{A28}$$

$$= -\frac{\vec{x}}{\varepsilon^3} \frac{(q \circ H)(\|\vec{x}\|)}{\left(H(\|\vec{x}\|) \right)^3} = -\frac{\vec{x}}{\|\vec{x}\|^3} q_\varepsilon(\|\vec{x}\|) \tag{A29}$$

A.3 | Time derivative of the integral over a time-varying domain

The aim of Appendix A.3 is to explain to the reader some mathematical aspects related to the time derivative of the left hand side term of Equation (22). This leads to Equation (A30):

$$\frac{\mathrm{d}}{\mathrm{d}t} \iiint_{\mathcal{P}_i(t)} \vec{\omega}\left(\vec{x},t\right) \mathrm{d}v\left(\vec{x}\right) = \iiint_{\mathcal{P}_i(t)} \left[\frac{\mathrm{D}\vec{\omega}}{\mathrm{D}t}\left(\vec{x},t\right) + \vec{\omega}\left(\vec{x},t\right)\left(\vec{\nabla}\cdot\vec{u}\right) \right] \mathrm{d}v\left(\vec{x}\right). \tag{A30}$$

Following Navier-Stokes continuity equation (Equation (1)), and with all the terms explicitly written, it is now clear that

$$\iiint_{\mathcal{P}_i(t)} \frac{\mathrm{D}\vec{\omega}}{\mathrm{D}t}\left(\vec{x},t\right) \mathrm{d}v\left(\vec{x}\right) = \frac{\mathrm{d}}{\mathrm{d}t} \iiint_{\mathcal{P}_i(t)} \vec{\omega}\left(\vec{x},t\right) \mathrm{d}v\left(\vec{x}\right) = \frac{\mathrm{d}\vec{\Omega}}{\mathrm{d}t}(t). \tag{A31}$$

This eventually explains Equation (22).

APPENDIX B: Implementation details of the lifting-line associated with a Lagrangian vortex particle method

B.1 | Dorothy LL-VP sub-iteration algorithm

1. Compute, for all p, the angle of attack $(\alpha(p,t))$ from Equation (28) and using Equation (27) with the true velocity $(\vec{u}_t(p,t)_{prev})$ value coming from either the initialization or the previous sub-iteration step.
2. Compute, for all k, the bound circulations based on Equation (30) with a relaxation factor $C = 0.3 \in [0,1]$:

$$\Gamma_B(k,t)_{new} = \Gamma_B(k,t)_{prev} + C\frac{1}{2}c(p)u_t(p,t)C_L(\alpha(p,t)), \quad p = 2k. \tag{B1}$$

3. Compute, for all k, the bound particles position, Equation (34), and vorticity weight, Equation (35).
4. Compute, for all n and for all j, the trailing shed particles position, Equation (36), and vorticity weight, Equation (37).
5. Compute, for all k, the spanwise shed particles position, Equation (38), and vorticity weight, Equation (40).
6. Compute, for all p, $\vec{u}_{near}^{\Psi}(p,t)$ which is the induction generated by those shed particles with Equation (17). It is reminded that the velocity radial component is forced to be zero. The velocity is updated according to this induction:

$$\vec{u}_t(p,t)_{new} = \underbrace{\vec{u}^{\infty} + \vec{u}(p,t) + \vec{u}_m(p,t) + \vec{u}_{wake}^{\Psi}(p,t)}_{\text{Already known}} + \vec{u}_{near}^{\Psi}(p,t)_{new} \tag{B2}$$

7. If the normalized criterion on the bound circulations e_{SI}, defined in Equation (B3), is higher than an user-defined threshold (e_0), generally $e_0 \simeq 10^{-3}$, go to step number 1.
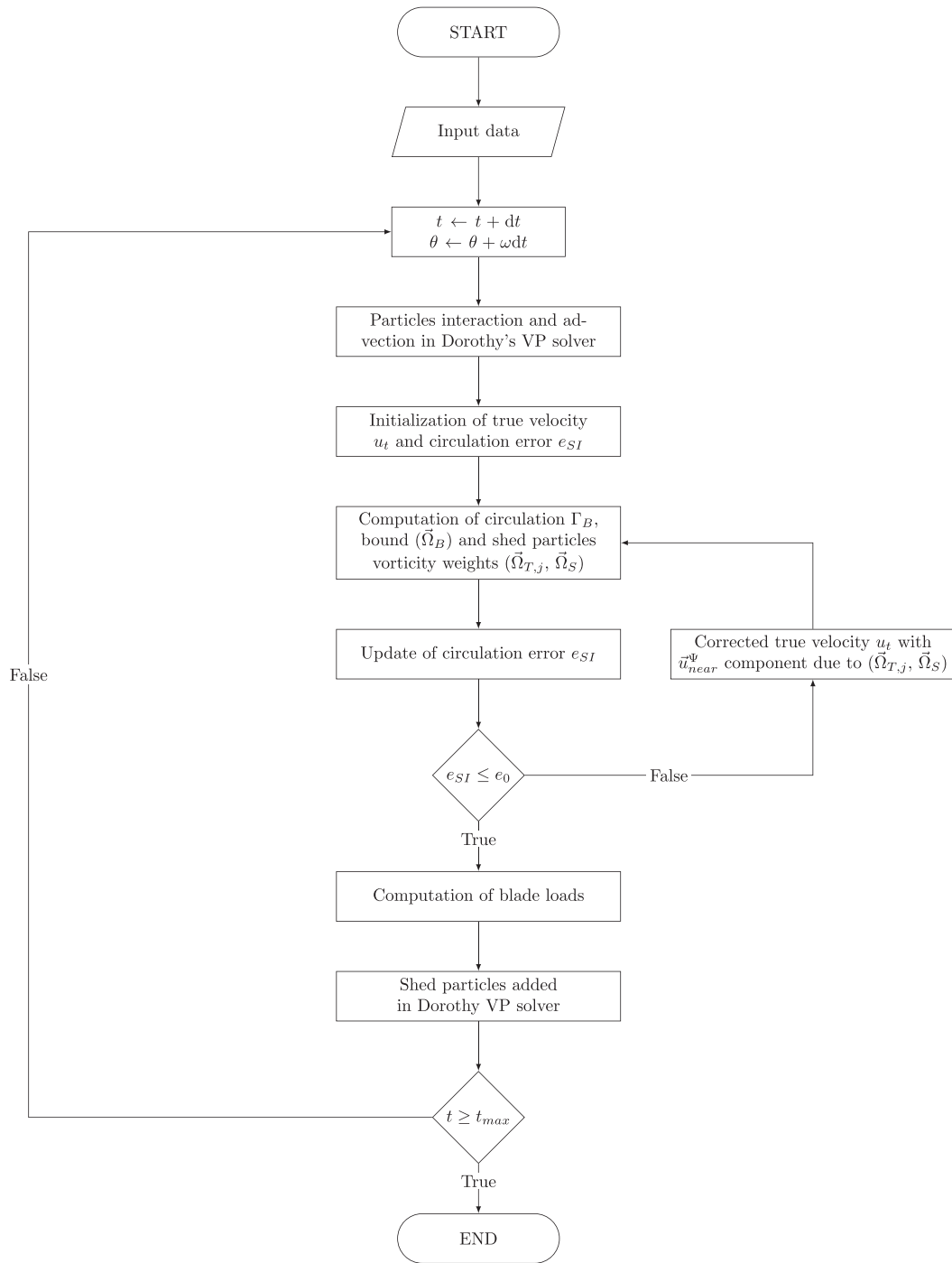
FIGURE B1   Dorothy LL-VP flowchart diagram.

$$e_{SI} = \max_{k} \left(\frac{|\Gamma_B(k,t)_{prev} - \Gamma_B(k,t)_{new}|}{\max\limits_{k}\left(\Gamma_B(k,t)_{prev}\right) + 1} \right) \tag{B3}$$

One is added to the normalizing factor to ensure that the denominator is different from zero.

B.2 | **Dorothy LL-VP general flowchart**

APPENDIX C: BLADE DESCRIPTION OF IFREMER-LOMC TIDAL TURBINE

Compared to the geometry originally published in Mycek et al,[64] a global pitch of 4.8743° is applied such that the pitch plus twist angle γ is zero at blade tip.

TABLE C1 Discrete description of IFREMER-LOMC tidal turbine blades.

| r/L (-)	c/L (-)	$-\gamma$ (°)	Profile (-)
0.000000	0.065280	24.6929	Cylinder
0.002155	0.065280	24.6929	Cylinder
0.021382	0.065280	24.6929	Cylinder
0.027138	0.065280	24.6929	Cylinder
0.076990	0.175115	20.753	NACA 63-422
0.126957	0.284836	17.2748	NACA 63-422
0.176809	0.273438	14.4288	NACA 63-422
0.226661	0.260082	12.0994	NACA 63-422
0.276628	0.246497	10.1795	NACA 63-422
0.326480	0.233602	8.5829	NACA 63-422
0.376332	0.221628	7.2426	NACA 63-422
0.426299	0.210576	6.1072	NACA 63-422
0.476151	0.200674	5.1371	NACA 63-422
0.526003	0.191694	4.3018	NACA 63-422
0.575970	0.183520	3.5773	NACA 63-422
0.625822	0.176036	2.9448	NACA 63-422
0.675674	0.169359	2.3895	NACA 63-422
0.725641	0.163257	1.8992	NACA 63-418
0.775493	0.157730	1.4644	NACA 63-418
0.825345	0.152549	1.0771	NACA 63-418
0.875313	0.147944	0.7307	NACA 63-418
0.925164	0.143569	0.4198	NACA 63-418
0.975016	0.139655	0.14	NACA 63-418
1.000000	0.075411	0	NACA 63-422
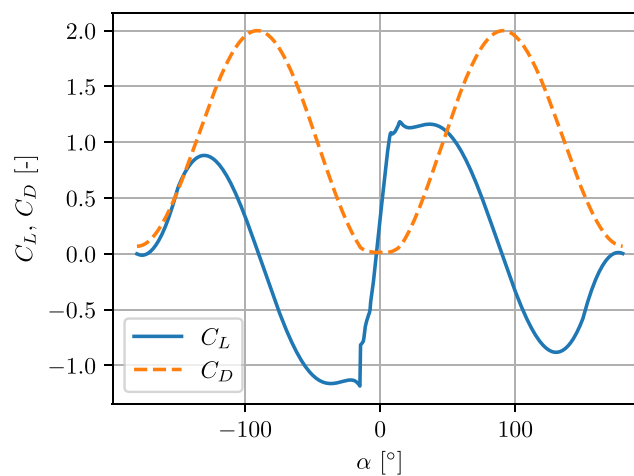
FIGURE C1 Full 360° angles of attack range NACA 63-418 polar curves computed at $Re = 2 \cdot 10^5$.